remote sensing

MDPI

Article

Contrasting the Performance of Eight Satellite-Based GPP Models in Water-Limited and Temperature-Limited Grassland Ecosystems

Liangxia Zhang [1,2], Decheng Zhou [1,2,*], Jiangwen Fan [3], Qun Guo [3], Shiping Chen [4], Ranghui Wang [1,2] and Yuzhe Li [3]

1 Jiangsu Key Laboratory of Agricultural Meteorology, Nanjing University of Information Science and Technology, Nanjing 210044, China; zhanglx@nuist.edu.cn (L.Z.); rhwang@nuist.edu.cn (R.W.)
2 Collaborative Innovation Center on Forecast and Evaluation of Meteorological Disasters, Nanjing University of Information Science and Technology, Nanjing 210044, China
3 Key Laboratory of Land Surface Pattern and Simulation, Institute of Geographic Sciences and Natural Resources Research, Chinese Academy of Sciences, Beijing 100101, China; fanjw@igsnrr.ac.cn (J.F.); guoq@igsnrr.ac.cn (Q.G.); liyuzhe@igsnrr.ac.cn (Y.L.)
4 State Key Laboratory of Vegetation and Environmental Change, Institute of Botany, Chinese Academy of Sciences, No. 20 Nanxincun, Xiangshan, Beijing 100093, China; spchen@ibcas.ac.cn
* Correspondence: zhoudc@nuist.edu.cn; Tel.: +86-25-58731539

Received: 28 April 2019; Accepted: 31 May 2019; Published: 3 June 2019

Abstract: Models constitute the primary approaches for predicting terrestrial ecosystem gross primary production (GPP) at regional and global scales. Many satellite-based GPP models have been developed due to the simple algorithms and the low requirements of model inputs. The performances of these models are well documented at the biome level. However, their performances among vegetation subtypes limited by different environmental stresses within a biome remains largely unexplored. Taking grasslands in northern China as an example, we compared the performance of eight satellite-based GPP models, including three light-use efficiency (LUE) models (vegetation photosynthesis model (VPM), modified VPM (MVPM), and moderate resolution imaging spectroradiometer GPP algorithm (MODIS-GPP)) and five statistical models (temperature and greenness model (TG), greenness and radiation model (GR), vegetation index model (VI), alpine vegetation model (AVM), and photosynthetic capacity model (PCM)), between the water-limited temperate steppe and the temperature-limited alpine meadow based on 16 site-year GPP estimates at four eddy covariance (EC) flux towers. The results showed that all the GPP models performed better in the alpine meadow, particularly in the alpine shrub meadow ($R^2 \geq 0.84$), than in the temperate steppe ($R^2 \leq 0.68$). The performance varied greatly among the models in the temperate steppe, while slight intermodel differences existed in the alpine meadow. Overall, MVPM (of the LUE models) and VI (of the statistical models) were the two best-performing models in the temperate steppe due to their better representation of the effect of water stress on vegetation productivity. Additionally, we found that the relatively worse model performances in the temperate steppe were seriously exaggerated by drought events, which may occur more frequently in the future. This study highlights the varying performances of satellite-based GPP models among vegetation subtypes of a biome in different precipitation years and suggests priorities for improving the water stress variables of these models in future efforts.

Keywords: gross primary productivity; light use efficiency model; satellite remote sensing; MODIS; EVI; eddy covariance; grassland ecosystem; temperate steppe; alpine meadow

1. Introduction

Gross primary production (GPP), defined as the sum of photosynthetic carbon uptake by vegetation, is the first step in the input of atmospheric CO_2 to terrestrial ecosystems [1,2]. An accurate estimation of GPP is essential for a better understanding of the ecosystem carbon cycle [3–5]. The eddy covariance (EC) method is an important tool for measuring land-atmosphere CO_2 exchange and thus the GPP of terrestrial ecosystems [6]. However, the applications of such a method are largely impeded by the limited number of flux tower sites and the limited spatial representativeness of their GPP estimates (i.e., footprint area) [7]. Models therefore constitute the primary approaches for predicting terrestrial ecosystem GPP over large areas [8,9].

Numerous models have been developed to estimate GPP from local to global scales [10,11]. Overall, these can be grouped into two broad types: process-based biogeochemical models and satellite-based models. The first simulates the full biogeochemical fluxes (e.g., carbon, water, and nitrogen cycles) on the basis of calculating key ecological processes, such as canopy interception and evaporation, transpiration, photosynthesis, growth and maintenance respiration, carbon allocation above and below-ground, litterfall, decomposition, and nitrogen mineralization [12]. They are usually driven by data, such as climate, soil, and land cover/use or vegetation specific parameters [13]. They have been widely used to simulate and predict carbon dynamics at different spatial scales [14]. However, such models may be subject to large errors, primarily due to (1) missing biogeochemical processes, (2) complex model structures, and (3) the uncertainties associated with the input data and parameters [15,16]. In contrast, satellite-based models simulate GPP based on simple algorithms [13,17]. They are mainly driven by satellite observations, which are only available historically and thus cannot predict future GPP [14,17]. Such models require few model inputs and parameters and can effectively address the spatial and temporal dynamics of GPP over large areas [17,18]. With advancements in remote sensing and spatial science, satellite-based models have been increasingly used to estimate GPP at various spatial scales in recent decades [9,17,18].

Many satellite-based GPP models have been developed and can be generally classified into two categories based on GPP algorithms: light-use efficiency (LUE) and statistical models. The LUE models were developed based on Monteith's production efficiency concept [19,20] and include the Carnegie-Ames-Stanford Approach (CASA) [21], the global production efficiency model (GLO-PEM) [22], the moderate resolution imaging spectroradiometer GPP algorithm (MODIS-GPP) [23,24], the vegetation photosynthesis model (VPM) [25,26], and the eddy covariance-light use efficiency (EC-LUE) model [27]. The modeled GPP corresponds to the product of the incident photosynthetically active radiation (PAR), the fraction of PAR absorbed by vegetation canopy (fPAR), the potential LUE without environmental stress (ε_{max}), and the reduction in LUE relative to ε_{max} due to environmental stresses (e.g., air temperature stress and water availability) (f). Different f scalars are usually used by different LUE models [9]. In contrast, statistical models estimate the GPP by its statistical relationship with greenness indices and/or environmental variables, and include the temperature and freenness (TG) model [28], the greenness and radiation (GR) model [29], and the vegetation index (VI) model [8]. These models often differ according to the environmental variables used.

The contrasting model structures and/or parameters result in large uncertainties in GPP estimates across the models and ecosystems [17,18,30,31]. For example, the environmental scalars of these GPP models were usually generated by the best-fit relationships between environmental indicators and the estimated GPP in a limited number of eddy flux sites [9,25,27,32,33]. They may not fully capture the actual relationship between a specific factor (e.g., moisture) and the GPP over a large area with substantial spatial heterogeneity [34]. In particular, the environmental stresses on GPP may vary considerably in a given biome under contrasting climate conditions [5]. In addition, a single environmental scalar cannot address the diverse responses of vegetation to environmental stresses, especially water stress, over large areas [3,17,33,34]. Moreover, the satellite-based GPP models do not consider interrelated physiological and ecological processes, and thus tend to neglect the exacerbated

effects of ecosystem responses during extreme climate events [35,36]. A comparison analysis of these models is critical for their effective application in estimating ecosystem GPP over large areas.

Previous efforts have focused mostly on the comparison of model performances among biomes [9,17,18,37,38]. The model performances were usually assumed to be the same among vegetation subtypes in a biome [38,39]. In fact, the carbon fixed by photosynthesis has varied considerably within biomes, and may be larger than that among different biomes [40], suggesting that the model performances may vary substantially inside a biome. This is especially true for the vegetation subtypes limited by contrasting environmental stresses. Although some studies have evaluated satellite-based GPP models at a vegetation subtype level, they have primarily concentrated on individual vegetation subtypes for specific research objectives [4,33,36,41–44]. In addition, previous studies have typically calibrated and evaluated the models by in situ observations during normal precipitation years [3,8,25,26,39]. A recent study highlighted that the biases in GPP estimates from the satellite-based models are governed by drought effects [45], indicating that model performances might have been overvalued in previous studies, particularly for areas experiencing frequent drought events. A systematic comparison of model performances among vegetation subtypes in different precipitation years is urgently needed for a better understanding of the satellite-based models, and would contribute to a better application of these models in global carbon cycle research.

Grasslands, occupying approximately one-fifth of the global land area [40], play a vital role in providing numerous ecosystem services such as regulating the global carbon cycle and supporting plant and animal biodiversity [46]. For example, grassland ecosystems store about 20% of total global carbon [47]. The status and distribution of grasslands therefore have gained strong interest from scientists and decision-makers and has been the subject of active research [46]. With the rapid advancement of space science and remote sensing techniques, satellite data have been widely used in grassland monitoring/observation, such as the grazing intensity, pasture quality and status, community classification, and carbon sequestration [46,48–52]. Among these, the GPP of grasslands has received considerable attention in recent decades due to its significance in understanding the ecosystem carbon cycle and the simplicity of satellite-based GPP models.

Using grasslands in northern China as an example, this study evaluated the performances of eight widely used satellite-based GPP models (VPM, MVPM, MODIS-GPP, TG, GR, VI, AVM, and PCM) using in situ GPP estimates at four EC flux towers covering two typical Chinese grassland subtypes (temperate steppe and alpine meadow). We hypothesized that the model performances were largely determined by their powers to explain environmental limitations. The specific objectives were to compare the model performances (1) between the temperate steppe and alpine meadow and (2) between the drought and non-drought years in the temperate steppe. The grasslands in northern China are ideal for comparisons of satellite-based GPP models among vegetation subtypes. First, they play an important role in both the global and China's national carbon budget due to their large area of coverage (33% of the total land in China) [40,53,54]. The northern China grasslands have been estimated to store 3.3%–10.1% of global grassland carbon [40,55] and approximately 7.1% of Chinese terrestrial carbon [56]. Second, the vegetation growth of temperate grassland and alpine grassland, the two major grassland types in northern China [57], are mainly controlled by water availability [58,59] and temperature [58,60], respectively. Third, the temperate grassland has experienced frequent extreme drought events during the past decades [61,62], and more severe droughts due to decreasing precipitation are projected in the next 30–90 years (e.g., the Palmer Drought Severity Index is projected to decrease by 0–7) [63,64]. Finally, the Chinese Terrestrial Ecosystem Flux Observation and Research Network (ChinaFLUX) [65] provides continuous carbon flux data in different grassland types, facilitating model comparisons among different grasslands and years. Our analyses will provide important insights for future efforts to improve satellite-based models in predicting terrestrial GPP at both regional and global scales.

2. Materials and Methods

2.1. Model Overview

The eight satellite-based GPP models, including three LUE models and five statistical models, are listed in Table 1. All these models have been applied in grassland ecosystems at either local and/or regional scales [3,4,9,38]. The EC-LUE model [27] was not included because the latent heat flux and sensible heat flux data required by the model were not available in this study. The CASA [21] and GLO-PEM [22] models were also not included in this study since the soil moisture data they require are difficult to obtain over large areas via either remote sensing or modeling methods [27].

Table 1. Model structures and parameters of the eight satellite-based gross primary production (GPP) models. LUE, light use efficiency.

Model	Type	fPAR	PAR	LUE(ε_g)	Calibrated Parameters	Input Data
Vegetation photosynthesis model (VPM) [25]	LUE	EVI	PAR	ε_{max}×ft×fw	ε_{max}, T_{min}, T_{opt}, T_{max}	EVI, PAR, Ta, LSWI
Modified VPM (MVPM) [9]	LUE	EVI	PAR	ε_{max}×min(ft, fw)	ε_{max}, T_{min}, T_{opt}, T_{max}	EVI, PAR, Ta, VPD, LSWI
MODIS-GPP algorithm (MODIS-GPP) [66]	LUE	MODIS-fPAR	PAR	ε_{max}×ft×fw	ε_{max}, $Tmin_{max}$, $Tmin_{min}$, VPD_{max}, VPD_{min}	MODIS-fPAR, SW_{rad}, T_{min}, VPD
Temperature and greenness model (TG) [28]	Statistical	f(EVI)	—	f(LST)	m	EVI, LST
Greenness and radiation model (GR) [29]	Statistical	EVI	PAR	—	m	EVI, PAR
Vegetation index model (VI) [8]	Statistical	EVI	PAR	EVI	m	EVI, PAR
Alpine vegetation model (AVM) [33]	Statistical	f(EVI)	—	f(Ta)	m, T_{min}, T_{max}	EVI, Ta
Photosynthetic capacity model (PCM) [39]	Statistical	f(EVI)	—	f(LST_{an})×fw	—	EVI, LST, LSWI

PAR, incident photosynthetically active radiation; fPAR, the fraction of PAR absorbed by vegetation canopy; EVI, enhanced vegetation index; ε_{max}, potential LUE without environmental stress; ft, effects of air temperature on ε_{max}; fw, effects of water availability on ε_{max}; T_{min}, T_{opt}, and T_{max} represent minimum, optimum, and maximum air temperatures for photosynthetic activities, respectively; Ta, air temperature; LSWI, satellite-derived land surface water index; VPD, vapor pressure deficit; $Tmin_{max}$, the daily minimum temperature at which $\varepsilon_g = \varepsilon_{max}$; $Tmin_{min}$, the daily minimum temperature at which $\varepsilon_g = 0$; VPD_{max}, the daylight average VPD at which $\varepsilon_g = \varepsilon_{max}$; VPD_{min}, the daylight average VPD at which $\varepsilon_g = 0$; m is a scalar determined by the model calibration; SW_{rad}, the incident shortwave radiation; LST, land surface temperature; LST_{an}, mean annual nighttime LST.

2.1.1. The Vegetation Photosynthesis Model (VPM)

VPM [25,26] assumes that the leaf and forest canopies consist of photosynthetically active vegetation and nonphotosynthetic vegetation that has been successfully used to simulate GPP in different ecosystems, including tropical evergreen forest [67], temperate deciduous forest [26], evergreen needleleaf forest [25], and cropland [68] at a site scale. The GPP in VPM is estimated as follows:

$$GPP = PAR \times fPAR \times \varepsilon_g \quad (1a)$$

$$fPAR = EVI \quad (1b)$$

$$\varepsilon_g = \varepsilon_{max} \times ft \times fw \quad (1c)$$

$$ft = \begin{cases} \frac{(T_a - T_{min})(T_a - T_{max})}{(T_a - T_{min})(T_a - T_{max}) - (T_a - T_{opt})^2} & (T_{min} < T_a < T_{max}) \\ 0 & (T_a < T_{min} \text{ or } T_a > T_{max}) \end{cases} \quad (1d)$$

$$fw = \frac{1 + LSWI}{1 + LSWImax} \times P_s \quad (1e)$$

$$P_s = \begin{cases} \frac{1+LSWI}{2} & (\text{before leaf full expansion}) \\ 1 & (\text{after leaf full expansion}) \end{cases} \quad (1f)$$

where ε_g represents the actual LUE, ft represents the effect of air temperature (T_a) on ε_{max}, and fw illustrates the water stress on ε_{max}. T_{min}, T_{max}, and T_{opt} represent the minimum, maximum, and optimum air temperatures for photosynthetic activities, respectively. EVI is the enhanced vegetation index, LSWI is the satellite-derived land surface water index, $LSWI_{max}$ is the maximum LSWI during

the growing season [25,26], and P_s indicates the phenology effect on $\varepsilon_{\max}$ [69]. In this study, P_s is set to 1.0 because the grassland canopies have new leaves emerging throughout the growing season [4]. LSWI is calculated via near-infrared (NIR, 841–875 nm) and shortwave infrared (SWIR, 1628–1652 nm) bands of MODIS images as follows:

$$LSWI = \frac{\rho_{NIR} - \rho_{SWIR}}{\rho_{NIR} + \rho_{SWIR}} \quad (1g)$$

2.1.2. The Modified VPM (MVPM)

Zhang et al. [9] suggested that VPM can be further improved by structural optimization. The MVPM was found to be better than the original VPM model for a wide range of ecosystem types [9]. The GPP in MVPM is expressed as follows:

$$GPP = PAR \times fPAR \times \varepsilon_g \quad (2a)$$

$$\varepsilon_g = \varepsilon_{max} \times \min(ft, fw) \quad (2b)$$

$$fw = W_s \times VPD_s \quad (2c)$$

$$VPD_s = \begin{cases} \frac{VPD_{max} - VPD}{VPD_{max}} & (VPD > 0.5 \text{ kPa}) \\ 1 & (VPD \leq 0.5 \text{ kPa}) \end{cases} \quad (2d)$$

where W_s and VPD_s represent the effects of soil moisture and atmospheric moisture conditions on GPP, respectively. fPAR and *ft* are the same as those in VPM (Equations (1b) and (1d)), and W_s is the same as *fw* in VPM (Equation (1e)). VPD_{max} is set to 3 kPa.

2.1.3. The MODIS GPP Algorithm (MODIS-GPP)

The latest MODIS-GPP product (MOD17A2H, version 6) [70] is driven by daily MODIS land cover, fPAR, leaf area index (LAI), interpolated surface meteorology, and the global vegetated land surface [66]. The MODIS-GPP is calculated as:

$$GPP = SW_{rad} \times 0.45 \times fPAR \times \varepsilon_g \quad (3a)$$

$$\varepsilon_g = \varepsilon_{max} \times f(Tmin) \times f(VPD) \quad (3b)$$

$$\text{f(Tmin)} = \begin{cases} 0 & Tmin < Tmin_{min} \\ \frac{Tmin - Tmin_{min}}{Tmin_{max} - Tmin_{min}} & Tmin_{min} < Tmin < Tmin_{\max} \\ 1 & Tmin > Tmin_{max} \end{cases} \quad (3c)$$

$$\text{f(VPD)} = \begin{cases} 0 & VPD > VPD_{max} \\ \frac{VPD_{min} - VPD}{VPD_{max} - VPD_{min}} & VPD_{min} < VPD < VPD_{max} \\ 1 & VPD < VPD_{min} \end{cases} \quad (3d)$$

where SW_{rad} represents the incident shortwave radiation and *f(Tmin)* and *f(VPD)* illustrate the minimum temperature stress and atmospheric moisture stress on GPP, respectively. $Tmin_{\max}$ is the daily minimum temperature at which $\varepsilon_g = \varepsilon_{\max}$, $Tmin_{\min}$ is the daily minimum temperature at which $\varepsilon_g = 0$, VPD_{max} is the daylight average VPD at which $\varepsilon_g = \varepsilon_{\max}$, and VPD_{min} is the daylight average VPD at which $\varepsilon_g = 0$. The values of $\varepsilon_{\max}$, $Tmin_{\max}$, $Tmin_{\min}$, VPD_{max}, and VPD_{min} varied among land use types and were obtained from the biome properties lookup tables. SW_{rad}, $T_{\min}$, and VPD were obtained from an updated version of the daily Global Modeling and Assimilation Office (GMAO) meteorological data, and fPAR were obtained from the MODIS LAI/fPAR products (MOD15A2).

2.1.4. The Temperature and Greenness model (TG)

The TG model [28] assumes that daytime land surface temperature (LST) was correlated with Ta, VPD, and PAR, and estimates GPP with EVI and LST as follows:

$$GPP = (scaledLST \times scaledEVI) \times m \tag{4a}$$

$$scaledLST = \begin{cases} \min\left[\left(\frac{LST}{30}\right), (2.5 - (0.05 \times LST))\right] & (0 < LST < 50) \\ 0 & (LST < 0 \text{ or } LST > 50) \end{cases} \tag{4b}$$

$$scaledEVI = EVI - 0.1 \tag{4c}$$

where the *scaledLST* is defined as the minimum of two linear equations. *ScaledLST* reaches a maximum of 1.0 when LST = 30 °C and a minimum of 0 when LST declines to 0 °C or increases to 50 °C. The *scaledLST* accounts for the drought conditions with high temperature and high VPD stress [28]. m is a scalar determined by the model calibration (the same for the other statistical models). The calculation method of m is detailed in Section 2.3.

2.1.5. The Greenness and Radiation Model (GR)

The GR model estimates GPP by EVI and PAR [29]. The basic assumption of the model is that EVI and PAR can represent the correlation between GPP and total canopy chlorophyll content [71–73]. The model has been successfully applied in irrigated and rainfed maize croplands [29,72], wheat croplands [74], and forests [75]. The GR model can be expressed as follows:

$$GPP = (EVI \times PAR) \times m \tag{5}$$

2.1.6. The Vegetation Index Model (VI)

The VI model estimates GPP using EVI and PAR and assumes that EVI is related to LUE and fPAR [8,29,74]. The model has been used in maize croplands and deciduous forest [8,74]. The VI model can be expressed as follows:

$$GPP = (EVI \times EVI \times PAR) \times m \tag{6}$$

2.1.7. The Alpine Vegetation Model (AVM)

AVM was developed by Li et al. [33] to estimate the GPP of alpine vegetation, which performs better than the VPM, TG, and VI models in alpine ecosystems. The AVM can be expressed as:

$$\text{GPP} = m \times EVI_{scaled} \times T_{scaled} \tag{7a}$$

$$EVI_{scaled} = EVI - EVI_{base} \tag{7b}$$

$$T_{scaled} = \frac{T - T_{min}}{T_{max} - T_{min}} \tag{7c}$$

where $\text{EVI}_{\text{scaled}}$ is used to represent the variance in fPAR, T_{scaled} is the temperature stress factor, and EVI_{base} is the mean value of EVI over time when the temperature is below the minimum temperature for photosynthetic activity (i.e., T_{min}). The photosynthetic process is expected to cease when the temperature falls below T_{min}.

2.1.8. The Photosynthetic Capacity Model (PCM)

PCM developed by Gao et al. [39] follows the logic of the LUE model and is driven by EVI and LSWI. The PCM model can be expressed as follows:

$$GPP = PC_{\text{max}} \times scaledEVI \times fw \tag{8a}$$

$$PC_{max} = 0.1346 \times LST_{an} + 2.7522 \quad (8b)$$

$$fw = (1 + \mathrm{LSWI})/2 \quad (8c)$$

where PC_{max} stands for the maximum photosynthetic capacity for a certain region (g C m^{-2} d^{-1}), scaledEVI represents the variability of photosynthetic capacity, and LST_{an} is the mean annual nighttime LST during the study period. The scaledEVI is the same as that in the TG model (Equation (4c)).

2.2. Data

2.2.1. Study Sites

Four EC tower sites covering the temperate steppe (NM and XL) and alpine meadow (GCT and SD) were selected for this study (Figure 1 and Table 2). The NM and XL sites are located at the Inner Mongolia Grassland Ecosystem Research Station (IMGERS) in the eastern Inner Mongolian Plateau, which has a semiarid continental climate. These two sites represent the typical grassland type in Inner Mongolia. The mean annual temperature (MAT) and precipitation (MAP) are 2 °C and 350 mm, respectively. Chestnut and dark chestnut soils were the zonal soil types found in this region [76]. Soil moisture is 0.18–0.26 m^3 m^{-3} and 0.05–0.07 m^3 m^{-3} are the field capacity and wilting point, respectively (http://www.chinaflux.org/). The GCT and SD sites are situated in the Haibei Alpine Meadow Ecosystem Research Station (HBAMERS) in the eastern Tibet-Qinghai Plateau, which has a plateau continental climate (MAT = –1.7 °C and MAP = 600 mm). These two sites represent the typical grassland type in the northeastern Tibet-Qinghai Plateau. The growing season temperature at these two sites (5–7 °C) is much lower than that in the temperate steppe (13 °C). Alpine shrub meadow (GCT) is distributed on mountain shadow slopes and dominated by mollic cryic cambisol soil with a high soil water content. Distributed in surface depressions, alpine swamp meadow (SD) is dominated by orthic spodosol soil, the soil surface of which is waterlogged with a water depth of approximately 0–5 cm during the growing season [77]. All four sites are member stations of the Chinese Terrestrial Ecosystem Flux Observational Network (ChinaFLUX), and detailed site information is available in Hao et al. [61], Chen et al. [78], and Li et al. [4].

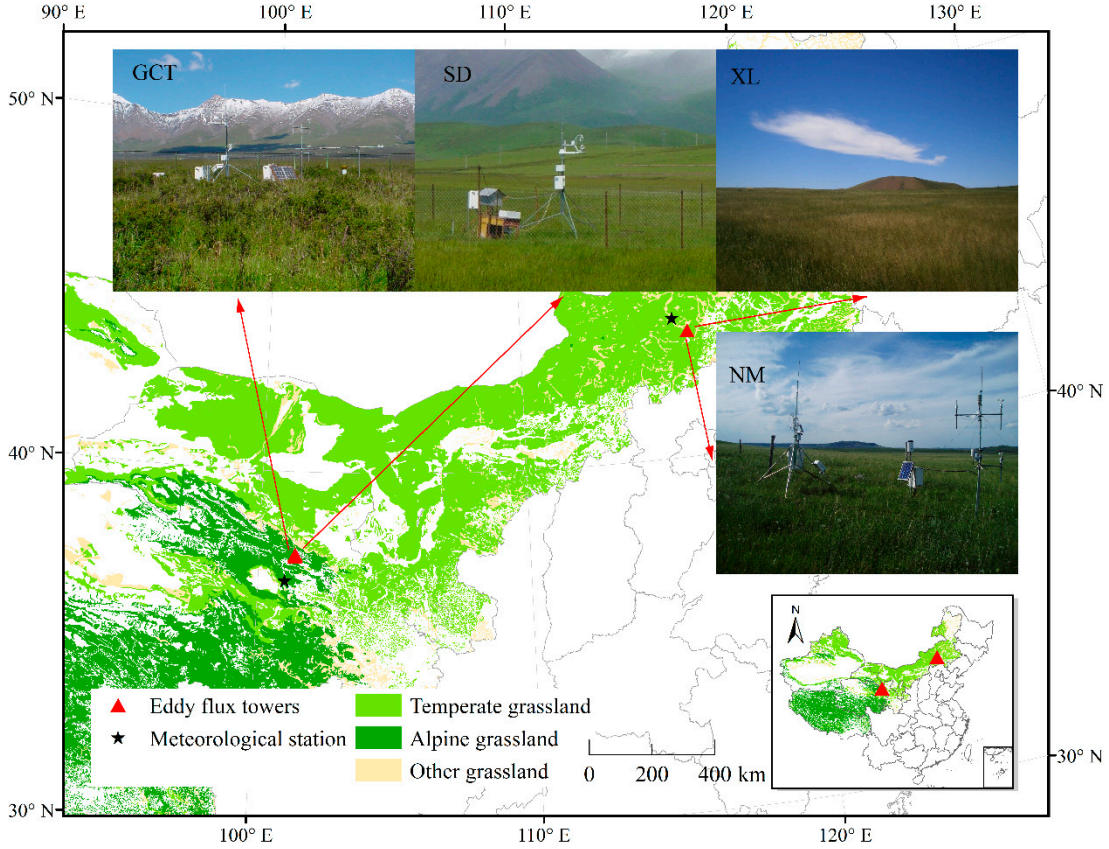

Figure 1. Geographic distribution and characteristics of the four grassland eddy flux tower sites in northern China.

Table 2. General information on the four grassland eddy flux tower sites in northern China.

Site	Lat, Lon, Alt (°N, °E, m)	Data Period	Vegetation Type	Dominant Species	Land Use	Reference
NM	43.55, 116.68, 1189	2004–2005	Temperate steppe	*Leymus chinensis*, *Stipa grandis*, *Agropyron cristatum*	Fenced since 1979	Hao et al. [61]
XL	43.55, 116.67, 1250	2006–2011	Temperate steppe	*Stipa grandis*, *Artemisia frigida*	Overgrazed before and fenced since 2005	Chen et al. [78]
GCT	37.67, 101.33, 3293	2003–2006	Alpine shrub meadow	*Potentilla fruticosa*, *Kobresia humilis*, *Festuca ovina*, *Elymus nutans*	Grazed in winter	Li et al. [4]
SD	37.61, 101.33, 3160	2003–2006	Alpine swamp meadow	*Kobresia tibetica*, *Pedicularis longiflora*	Grazed in winter	Li et al. [4]

2.2.2. GPP and Meteorological Data

The daily GPP and meteorological data (T_a, VPD, and PAR) at the four sites were acquired from the ChinaFLUX website (http://www.chinaflux.org/) [65,79]. These data represent the region of the footprint area of the flux sites (ca. 250 × 250 m). The daily GPP was calculated as the sum of the net ecosystem CO_2 exchange and ecosystem respiration. More information can be found at Yu et al. [65] and Chen et al. [78]. The daily GPP and meteorological measurements were averaged to an eight-day interval to match the temporal resolution of the MODIS data. The model comparisons of this study were conducted in the growing season only, to exclude possible spurious satellite observations during the nongrowing season [80,81]. The growing seasons for the four sites were defined by the phenology observation data at nearby meteorological stations (Figure 1). The meteorological data were obtained from the China Meteorological Data Service Center (http://data.cma.cn/). The years 2005, 2006, and 2009 were identified as drought years in the temperate steppe according to Guo et al. [60]. Guo et al. [60]

identified these drought years based on the characteristics of precipitation events (e.g., size, frequency, interval, and seasonal distribution of precipitation events). The drought years can also be identified from MODIS evapotranspiration (ET) observations (MOD16A2, 500 m, version-6) [82]. For example, the growing season ET in 2005, 2006, and 2009 was clearly lower than that in the other years for the two temperate steppe sites (NM and XL) (Figure 2). The growing season lengths were similar for the drought (176 ± 23.6 days) and non-drought (171 ± 19.3 days) years in the temperate sites, suggesting that the growing season length had little influence on the annual GPP.

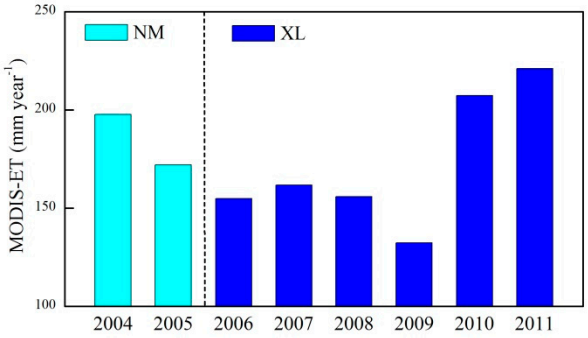

Figure 2. MODIS evapotranspiration (ET) observations for the two temperate steppe sites (NM and XL) during the growing season from 2004 to 2011.

2.2.3. MODIS Products

Version-6 MODIS eight-day surface reflectance composite data (MOD09A1, 500 m) [83], LST product (MOD11A2, 1000 m) [84], and GPP products (MOD17A2H, 500 m) [70] were used in this study. The pixel values in which the flux towers were located were acquired from MODIS Land Product Subsets at ORNL DAAC (https://modis.ornl.gov/cgi-bin/MODIS/global/subset.pl). The surface reflectance composite data were utilized to calculate LSWI as Equation (1g) and EVI as follows:

$$EVI = 2.5 \times \frac{\rho_{NIR} - \rho_{Red}}{\rho_{NIR} + 6 \times \rho_{Red} - 7.5 \times \rho_{Blue} + 1} \quad (9)$$

where ρ_{Blue} and ρ_{Red} are the surface reflectance values of blue (459–479 nm) and red (620–670 nm), respectively. The daytime (10:30 am) and nighttime (10:30 pm) LST digital number (DN) values were converted to temperature (°C unit) using the equation below:

$$LST = DN \times 0.02 - 273.15 \quad (10)$$

The GPP products were generated by the Numerical Terradynamic Simulation Group (NTSG), University of Montana (UMT) [70]. The algorithms are presented in Section 2.1.3. The missing or unreliable values with the "F" flag due to failed quality control (QC) criteria were temporally filled in by the linear interpolation method [18,85,86].

2.3. Model Calibration

All models required calibration, except for PCM. Site-specific data were used to calibrate them. Calibration of the VPM and MVPM models involves the estimations of $\varepsilon_{\max}$, $T_{\min}$, T_{opt}, and $T_{\max}$. The values of $T_{\min}$, T_{opt}, and $T_{\max}$ vary among vegetation types [25]. The $T_{\min}$, T_{opt}, and $T_{\max}$ in the temperate steppe (NM and XL) were set to −2, 20, and 35 °C, respectively [87], and those in the alpine meadow (GCT and SD) were set to 0, 20, and 35 °C, respectively [4]. The site-specific $\varepsilon_{\max}$ is usually estimated by the nearly instantaneous (e.g., half-hourly scale) net ecosystem CO_2 exchange (NEE) and photosynthetic photon flux density (PPFD) during the peak growth stage [26,88,89]. We used $\varepsilon_{\max}$ values of 0.30 g C mol^{-1} PPFD, 0.41 g C mol^{-1} PPFD, and 0.38 g C mol^{-1} PPFD for the NM, GCT,

and SD sites, respectively [4,36]. To stay in accordance with the other sites, the ε_{max} value for the XL site was estimated by one week of half-hourly flux data during peak growth periods (16–22 July 2011). The one-week period was selected based on the maximum daily NEE during 2006–2011. The ε_{max} was calculated using the Michaelis–Menten function [89] as follows:

$$NEE = \frac{\varepsilon_{max} \times PPFD \times GPP_{max}}{\varepsilon_{max} \times PPFD + GPP_{max}} - R_{dark} \quad (11)$$

where GPP_{max} is the maximum canopy CO_2 uptake rate at light saturation, and R_{dark} is the mitochondrial CO_2 respiration in the dark. ε_{max}, GPP_{max}, and R_{dark} are the fitted parameters with half-hourly observed NEE and PPFD data using nonlinear regression analysis (Figure 3). The ε_{max} was estimated to be 2.1 g CO_2 mol^{-1} PPFD or 0.57 g C mol^{-1} PPFD for the XL site.

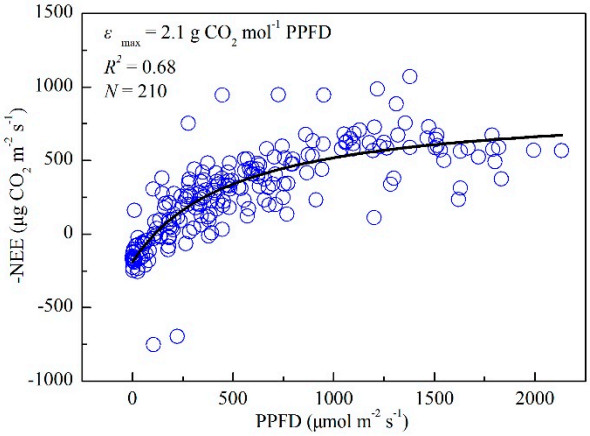

Figure 3. Light-response curve function on 16–22 July 2011, at the XL site.

Calibration of the TG, GR, VI, and AVM models primarily involves the estimation of the scalar *m*. In practice, they can be calibrated using a half-data method (with the remaining data for model validation) [28,72] or an all-data method (all the data are used for both the model calibration and validation) [18,90]. In this study, we used the all-data calibration since the half-data method may result in large uncertainties in the model performances if using short-term observations [18,90]. For example, only two years of flux data are available for the NM site. In addition, the half-data method would make the LUE and statistical models noncomparable due to the different amounts of validation data.

2.4. Evaluation of Model Performance

The predicted GPPs were evaluated against the EC estimates (GPP_tower) at an eight-day interval during the growing season. The alpine shrub meadow (GCT) and alpine swamp meadow (SD) sites were analyzed separately due to their highly contrasting soil conditions. The model performances in the two temperate steppe sites (NM and XL) were evaluated together due to (1) their similar environmental conditions and (2) the limited EC observations in the NM site. The correlation coefficient (R^2), root mean squared error (RMSE, %) [38], percent bias (PBIAS, %) [91], and corrected Akaike Information Criterion (AICc) [80,92] were used to evaluate the model performance. The higher the R^2, and the lower the RMSE and AICc, the better the model performance. The RMSE, PBIAS, and AICc are calculated as follows:

$$RMSE = \frac{100}{\overline{O}} \times \sqrt{\frac{\sum (M_i - O_i)^2}{N}} \quad (12)$$

$$PBIAS = \frac{\sum (M_i - O_i) \times 100}{\sum O_i} \quad (13)$$

$$AIC_C = N \times \ln(\frac{RSS}{N}) + 2K + \frac{2K \times (K+1)}{N-K-1} \quad (14)$$

where $\overline{O}$ is the average of the observed values, O_i and M_i represent the observed and modeled GPP, respectively, and N indicates the total number of estimates at the study site. The optimal value of PBIAS is 0, while positive and negative values suggest an underestimation and an overestimation of GPP, respectively. K is the number of parameters fit by the regression plus 1, and RSS is the residual sum of squares of the model. Since the AICc is an estimator of the relative quality of statistical models for a given set of data, it was only applied to examine the inter-model differences in this study.

We also compared the modeled and observed GPP at an annual scale to evaluate the capability of these models to capture the interannual patterns of GPP. Given that a single environmental scalar may not fully capture the environmental stresses over the temperate steppe and alpine meadow, stepwise multiple linear regressions were developed between the observed GPP and all the variables used by these satellite-based models (i.e., EVI, Ta, LSWI, PAR, LST, and VPD) to calculate the independent and total explanation powers of them with the GPP's variability.

3. Results

3.1. Seasonal and Interannual Variations in Climate, GPP, and Vegetation Indices at the Four Flux Tower Sites

The climatic conditions differed dramatically between the temperate steppe sites (NM and XL) and the alpine meadow sites (GCT and SD) (Figure 4). The temperate steppe sites were characterized by a dry-warm climate, with a growing season precipitation and mean temperature of 219 mm and 14 °C, respectively, whereas the alpine meadow sites were dominated by a humid-cold climate, with precipitation and temperature of 465 mm and 6 °C, respectively. The drier climate in the temperate steppe compared with that in the alpine meadow can also be viewed in terms of soil water content (SWC) (0.12 vs. 0.26 m^3 m^{-3}, respectively) and vapor pressure deficit (VPD) (9.75 vs. 3.13 hPa, respectively). In addition, precipitation and SWC varied greatly by year in the temperate steppe sites. For example, the growing season precipitation in 2005 was less than half of that in 2004 (153.3 vs. 354.5 mm yr^{-1}, respectively) at the NM site. There were clearly more heavy rainfall events in the peak growing season (180–240 days of year) in 2007, 2008, 2010, and 2011 than in 2006 and 2009 for the XL site.

The observed GPP, fPAR, EVI, NDVI, and LSWI were higher in the alpine meadow than in the temperate steppe during the growing season (Figure 5). For example, the annual GPP and mean EVI of the alpine meadows were 37.4% and 76.1% higher, respectively, than those of the temperate steppe (453.5 vs. 330 g C m^{-2} yr^{-1}, respectively, for the annual GPP, and 0.34 vs. 0.19, respectively, for the mean EVI). Generally, the seasonal patterns of GPP were similar to those of the EVI, NDVI, LSWI, and MODIS-fPAR in all four sites. However, none of the indices captured the sharp reduction in GPP (Figure 5a,b) caused by the flash drought (almost no precipitation from late June to early July) and warm temperatures during the peak growing season in 2004 at the NM site and in 2007, 2008, and 2010 at the XL site. Inconstant patterns were also observed in the XL site during the drought years (Figure 5b). For example, the observed GPP peaked more than one month earlier than that shown by all the vegetation indices in 2006. Surprisingly, the alpine meadow sites showed clear dips in MODIS-fPAR during some years, possibly due to the poor quality of data from the growing season.

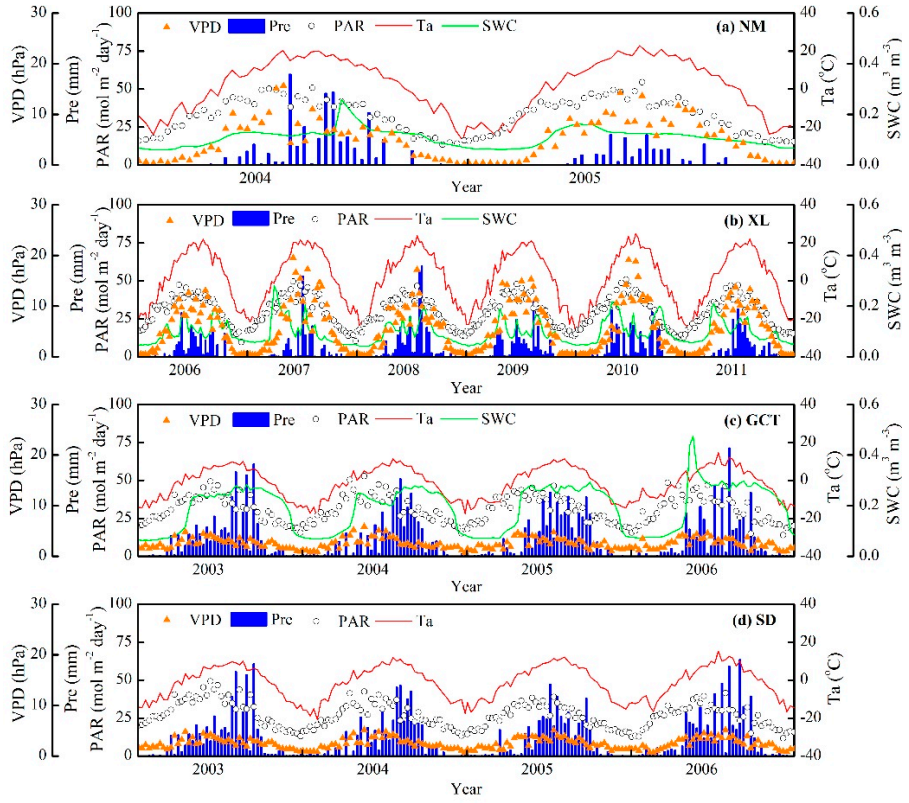

Figure 4. Seasonal and interannual variations in precipitation (Pre), air temperature (Ta), vapor pressure deficit (VPD), photosynthetically active radiation (PAR), and soil water content (SWC) at the (**a**) NM, (**b**) XL, (**c**) GCT, and (**d**) SD flux tower sites. SWC was measured at depths of 0–20 cm at the NM and GCT sites and 0–10 cm at the XL site. SWC was not measured at the SD site due to the waterlogged soil surface.

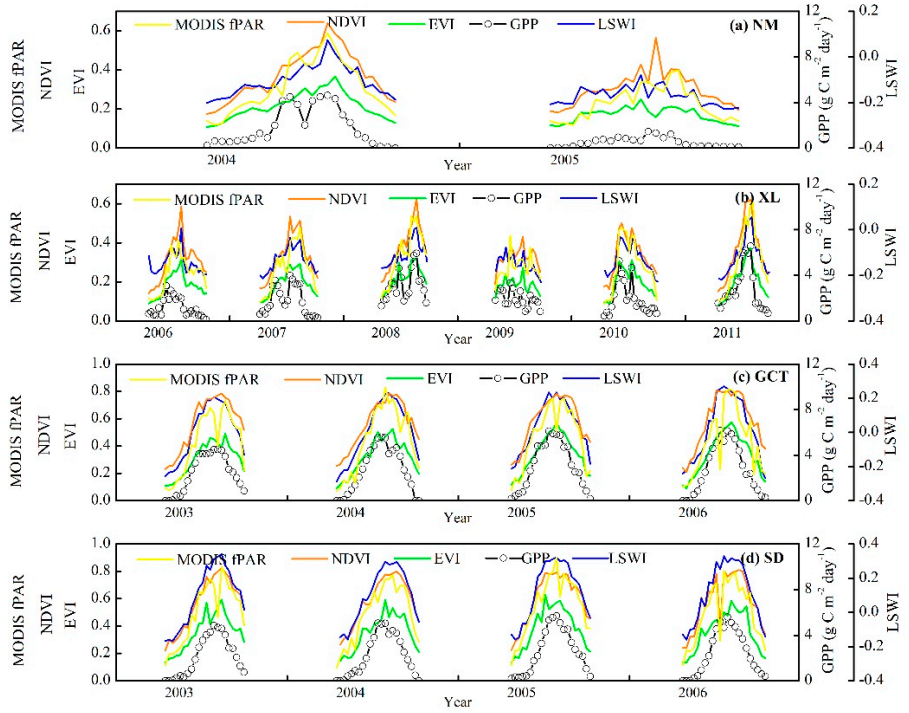

Figure 5. Seasonal and interannual variations in the observed gross primary production (GPP_tower), fraction of the absorbed photosynthetically active radiation (fPAR), normalized difference vegetation index (NDVI),

enhanced vegetation index (EVI), and land-surface water index (LSWI) at the (**a**) NM, (**b**) XL, (**c**) GCT, and (**d**) SD flux tower sites.

Interannually, GPP in the temperate steppe sites showed much larger variation throughout the year (Figure 5) and a closer relationship ($p < 0.01$) with the vegetation indices (i.e., EVI, NDVI, and LSWI) (Figure 6) than that in the alpine meadow. However, GPP decreased more rapidly than the other variables during the severe drought years (i.e., 2005, 2006, and 2009) in the temperate steppe. For example, GPP in 2005 was 73.1% lower than that in 2004 when the EVI declined by only 21.6%. Interestingly, no significant relationships were observed between GPP and climate variables (e.g., Ta, Prec, VPD) in either of the grassland subtypes, possibly due to the limited number of observation years. However, GPP was more closely related to the temperature-related variables (Ta and LST) than the moisture-related indicators (Prec and SWC) in the alpine meadow sites. The opposite relationships were found in the temperate steppe. These results partially prove the dominant role of water stress and temperature stress on GPP in the temperate steppe and alpine meadow, respectively [58–60,93].

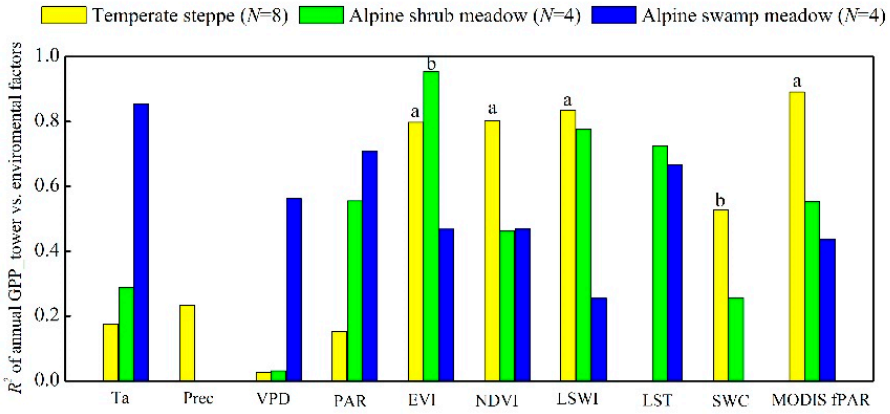

Figure 6. Correlations between the observed GPP (GPP_tower) and the climate variables or vegetation indices throughout the year. The observations at the two temperate steppe sites (NM and XL) were analyzed together since (1) they were observed in different years and (2) only two years of data were available for the NM site. [a], significant at the 0.01 level; [b], significant at the 0.05 level.

3.2. Comparison of the Eight Satellite-Based GPP Models in Estimating GPP between the Temperate Steppe and Alpine Meadow

All of the models performed much better in the alpine shrub meadow ($R^2 \geq 0.84$) and alpine swamp meadow ($R^2 \geq 0.70$) than in the temperate steppe ($R^2 \leq 0.68$) as compared with the site-level observations (Table 3). The mean explanatory power of these eight models reached 89%, 82%, and 61% in the alpine shrub meadow, alpine swamp meadow, and temperate steppe, respectively. Additionally, the RMSEs of the alpine shrub meadow (25.8%) and alpine swamp meadow (35.9%) were clearly smaller than that of the temperate steppe (56.7%).

The performance varied greatly among the models in the temperate steppe. The MVPM and VI models with higher R^2 and lower AICc were the two better-performing models (R^2 = 68% and 67%, respectively, and AICc = –40.4 and –54.7, respectively) of the LUE and statistical models, respectively. The AVM, VPM, and PCM performed relative poorly ($R^2 \leq 60\%$ and AICc ≥ 5.9). In contrast, slight intermodel differences were observed in the alpine meadow. The MODIS-GPP and GR performed relatively worse ($R^2 \leq 0.84$, RMSE ≥ 24.5%) than the other LUE and statistical models (R^2 = 0.88–0.91, RMSE = 22.6%–27.4%), respectively. GPP estimates were close to the EC observations for most models regardless of grassland type (|PBIAS| < 16.5%), except for a significant overestimation by the VPM in the temperate steppe (54.2%) and by the PCM in the alpine swamp meadow (31.0%), and an obvious underestimation by the PCM in the temperate steppe (40.6%). Overall, the performances of the LUE

models (VPM, MVPM, and MODIS-GPP) were slightly worse than those of the statistical models (TG, GR, VI, AVM, and PCM) (Table 3), with a mean R^2 of 0.72 and 0.75, respectively. Nevertheless, the best-performing LUE model (MVPM) and statistical model (VI) had similar modeling performance, characterized by R^2 values of 0.80 and 0.79, respectively, AICc values of –153.4 and –150.4, respectively, and RMSE values of 36.5% and 36.9%, respectively.

Table 3. Performances of the VPM, MVPM, MODIS-GPP, TG, GR, VI, AVM, and PCM in estimating GPP over the temperate steppe and alpine meadow as reflected by R^2, RMSE (%), PBIAS (%) and AICc validation. *N* represents the number of data points.

Model Type	Model Performance Indices	Model	Temperate Steppe			Alpine Shrub Meadow (*N* = 90)	Alpine Swamp Meadow (*N* = 90)	All Site Years (*N* = 271)
			Drought (*N* = 69)	Non-Drought (*N* = 112)	All (*N* = 181)			
LUE	R^2	VPM	0.54	0.61	0.59	0.91	0.86	0.64
		MVPM	0.50	0.75	0.68	0.91	0.81	0.80
		MODIS-GPP	0.37	0.66	0.60	0.84	0.81	0.73
		Average	0.47	0.67	0.62	0.89	0.83	0.72
	RMSE (%)	VPM	140.2	65.9	83.5	27.4	30.4	54.9
		MVPM	81.7	36.7	47.4	22.6	34.5	36.5
		MODIS-GPP	88.4	41.9	52.9	31.6	37.6	42.2
		Average	103.4	48.2	61.3	27.2	34.2	44.5
	PBIAS (%)	VPM	108.7	37.4	54.2	16.5	6.2	16.0
		MVPM	53.6	−1.5	11.5	5.7	4.3	4.2
		MODIS-GPP	50.5	−2.5	10.0	−12.2	14.2	4.2
		Average	70.9	11.1	25.2	3.3	8.2	8.1
	AICc	VPM	74.2	99.0	162.3	−42.5	−49.4	138.6
		MVPM	2.0	−29.8	−40.4	−75.1	−24.7	−153.4
		MODIS-GPP	10.5	−2.6	−3.0	−16.8	−13.6	−52.9
Statistical	R^2	TG	0.47	0.66	0.61	0.89	0.84	0.78
		GR	0.50	0.65	0.61	0.89	0.70	0.74
		VI	0.46	0.72	0.67	0.89	0.78	0.79
		AVM	0.43	0.57	0.54	0.88	0.88	0.76
		PCM	0.28	0.65	0.60	0.88	0.86	0.66
		Average	0.43	0.65	0.61	0.89	0.81	0.75
	RMSE (%)	TG	73.4	43.1	50.4	24.0	32.2	37.7
		GR	72.0	43.5	50.4	24.5	43.9	41.0
		VI	69.6	38.8	46.1	24.0	37.1	36.9
		AVM	75.3	48.0	54.8	25.3	27.7	39.1
		PCM	70.5	64.3	68.0	27.0	43.7	49.7
		Average	72.2	47.5	53.9	25.0	36.9	40.9
	PBIAS (%)	TG	34.5	−10.6	0.0	0.4	1.3	0.5
		GR	36.2	−10.3	0.7	0.2	0.9	0.6
		VI	26.9	−8.1	0.2	0.0	0.0	0.1
		AVM	36.9	−11.0	0.3	0.0	0.0	0.1
		PCM	−25.1	−45.4	−40.6	−8.4	31.0	−11.4
		Average	21.9	−17.1	−7.9	−1.6	6.6	−2.0
	AICc	TG	−19.7	−0.6	−24.7	−70.7	−46.3	−139.6
		GR	−22.4	1.6	−24.3	−67.0	9.6	−77.8
		VI	−24.9	−22.1	−54.7	−68.8	−18.5	−150.4
		AVM	−16.1	23.7	5.9	−61.2	−73.5	−111.8
		PCM	−25.2	89.1	84.0	−49.8	8.7	59.9

In addition, the performances of all the models were much poorer in drought years than in non-drought years in the temperate steppe (Table 3). The mean R^2 of all the models in non-drought years was 32.6% higher than that in severe drought years. The explanatory powers of the two best-performing models (MVPM and VI) were 33.3% and 36.1% lower in drought years than in non-drought years, respectively. The RMSEs were also much larger in drought years than in non-drought years for the MVPM (81.7% vs. 36.7%, respectively) and VI (69.6% vs. 38.8%, respectively) models. All the models except the PCM overestimated the GPP significantly (26.9%–108.7%) in the drought years. Furthermore, the relative qualities of these eight models in the drought years (as reflected by AICc) were different from that during non-drought years (Table 3). For example, though the VPM model had the highest R^2, it was the worst because it had the largest RMSE.

On an annual scale, the GPP estimates differed greatly by model in the temperate steppe. Only three models (MVPM, TG, and VI) could capture the interannual variations in GPP ($R^2 \geq 0.53$,

$p < 0.05$, $N = 8$) (Figure 7a). Overall, the percent biases of the VPM and PCM (|PBIAS| > 40.6%) were much larger than those of the other models (|PBIAS| < 11.5%). The VPM and PCM overestimated (18.8%–175.6%) and underestimated (28.1%–55.0%) the GPP substantially at the two temperate steppe sites (i.e., NM and XL) during most of the study years. In addition, all the models overestimated the annual GPP by 36.7%–215% in the two drought years (2005 and 2006), except for an underestimation by the PCM in 2006. Notably, the estimates from the MODIS-GPP were as much as 2.1 times that of the GPP_tower in 2005. As a result, the drought-induced reductions in the GPP were significantly underestimated by all the GPP models. For example, the observed GPP decreased by 73.1% from 2004 to 2005, which was clearly larger than the decrease in the simulated GPP (24.6%–55.3%). Comparatively, the annual GPP estimates from all the models varied slightly and were close to in situ observations (|PBIAS| < 26.8%) at the two alpine meadow sites (Figure 7b,c). Notably, the observed GPP in the alpine swamp meadow increased slightly by 6.2%, but the GPP estimated by the VPM, MVPM, GR, and VI models decreased significantly by more than 14.5% in 2004 relative to 2003.

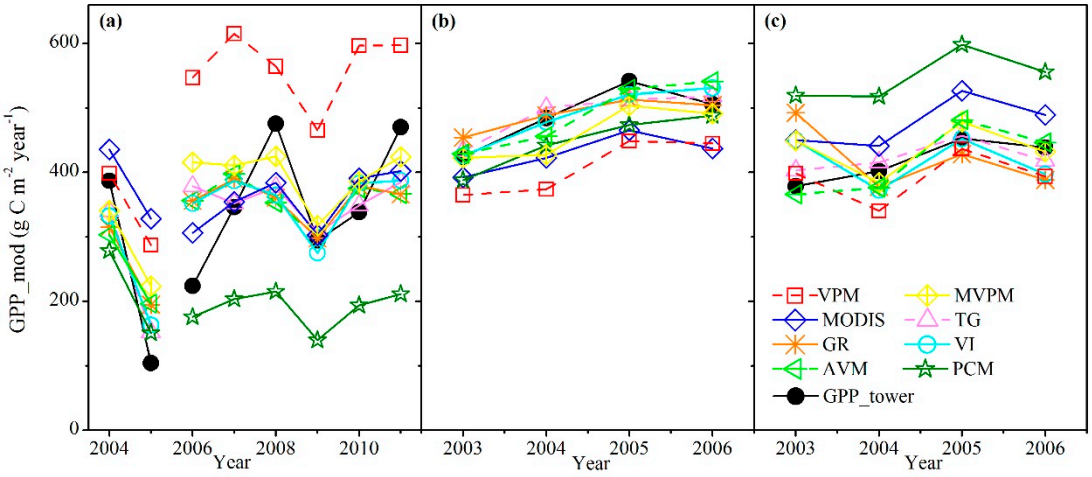

Figure 7. Comparisons of the modeled annual GPP with observations in the (**a**) temperate steppe, (**b**) alpine shrub meadow, and (**c**) alpine swamp meadow.

Table 4 shows the comparison between the explanation rates of a single variable (to the GPP's fluctuations) derived from linear regressions and the independent explanation rate of each variable, as well as the total derived from stepwise multiple linear regression. Results showed that the combination of multiple variables explained the much higher variability of GPP than any single factor over the temperate steppe and alpine meadow. For example, the total explanation power of EVI, Ta, LSWI, PAR, LST, and VPD was 18.4% higher than that of the best predictor (i.e., EVI) (76% vs. 62%, respectively).

Table 4. Explanation rate (%) of a single variable of the GPP's fluctuations derived from linear regressions and the independent explanation rate and total explanation rate (%) of each variable derived from stepwise multiple linear regression at the four grassland eddy flux tower sites. [a], significant at the 0.01 level; [b], significant at the 0.05 level.

Variables	EVI	Ta	LSWI	PAR	LST	VPD	Combined
Explanation rate	62 [a]	11 [a]	50 [a]	1	0	1	—
Independent explanation rate	66 [a]	5 [a]	2 [a]	1 [a]	2 [a]	1 [b]	76

4. Discussion

4.1. Varying Performances of the Eight Satellite-Based GPP Models between the Temperate Steppe and Alpine Meadow

As expected, our results showed that all eight satellite-based GPP models performed better in the temperature-limited alpine meadow than in the water-limited temperate steppe. The large uncertainties in the GPP models in the dry climate were highly consistent with previous findings [3,17,94,95], and can be mainly attributed to the poor representation of the effect of water stress on GPP in these models [17,34,96]. First, the environmental variables (e.g., EVI, LST, Ta, LSWI, and VPD) in these models cannot fully address the soil water content (SWC) dynamics that mainly determine water availability to plants [53,59,60]. For example, the decreases in the EVI usually lag behind the SWC when drought occurs [18,53]. The VPD (LSWI) is more closely related to atmospheric water content [9,97,98] (leaf water content [25]) than to the SWC [27,99]. The LST and Ta may even increase during extreme drought events [53]. Recent studies have indicated that solar-induced chlorophyll fluorescence (SIF) and other improved vegetation indices (i.e., normalized difference drought index and Normalized Multi-band Drought Index) are more sensitive to drought than EVI or LSWI [100–103], which may serve as a potential direction for future model improvements. Second, the linear functions in these models may not fully capture the complex photosynthetic responses to water stress in arid regions [104]. These can be partially verified by the much weaker correlations between the observed GPP and fPAR/LUE of the LUE models or by multiplication of the environmental factors of the statistical models in the temperate steppe than in the alpine meadow (Figure 8). Furthermore, previous studies have typically used a single function of environmental indicators to reflect the moisture stress for all grassland types [3,38,39]. In fact, the responses of photosynthesis to moisture stress vary greatly by grassland type [34,105]. For example, in the arid temperate steppe, vegetation with shallow roots would experience stomatal closure to avoid water loss if soil water was limited [53]. In contrast, humid alpine meadow vegetation would likely extract deep soil water by increasing the root length if the surface soil moisture was limited due to drought occurrences and/or a period of warming (one or more years) [106–108]. The function of environmental indicators was mostly generated by the best-fit relationship between the environmental variables and GPP in the limited tower sites covering humid or semihumid ecosystems [8,25,33], which would exaggerate the uncertainties of the GPP estimates in the water-limited areas [34].

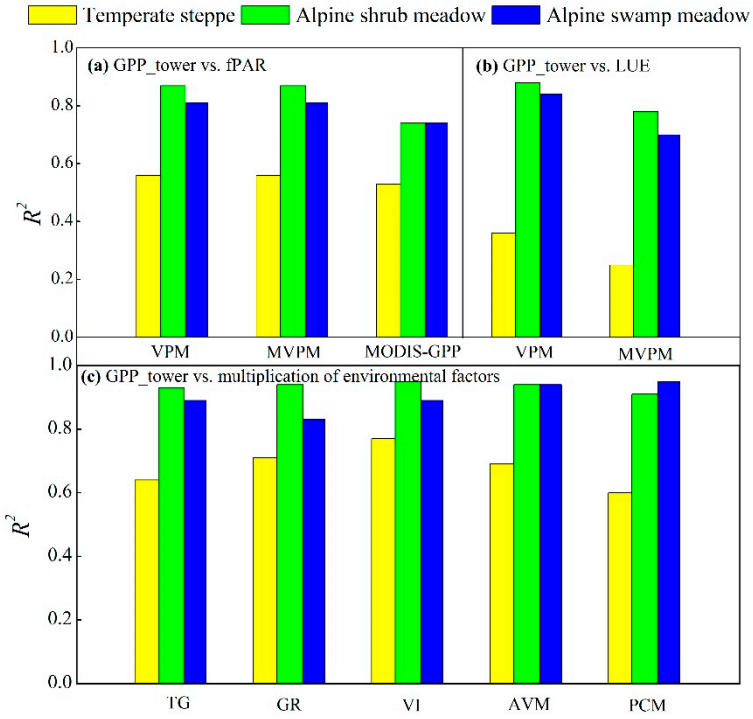

Figure 8. The R^2 of (**a**) GPP_tower vs. fPAR, (**b**) GPP_tower vs. LUE for the three LUE models and (**c**) GPP_tower vs. multiplication of environmental factors for the five statistical models in the temperate steppe, alpine shrub meadow, and alpine swamp meadow ($p < 0.01$). The R^2 value between the GPP_tower and LUE for MODIS-GPP was not calculated due to the unavailability of the LUE data used by the model. The multiplication of environmental factors for the TG, GR, VI, AVM, and PCM are EVI × Scaled_LST, EVI × PAR, EVI × EVI × PAR, EVI × Ta, and EVI × LSWI, respectively.

In addition, most GPP models performed better in the alpine shrub meadow than in the alpine swamp meadow. This phenomenon can be attributed to two factors. One is that these models cannot reflect the slight depression of surface water on GPP in the alpine swamp meadow. The surface water could decrease the amount of aerial biomass, which plays a key role in photosynthesis and thus decreases CO_2 uptake by the emergent plants [109]. However, all these GPP models assume a higher GPP with more water. The other factor is that these GPP models may aggregate the effects of the PAR on GPP, which was reported not to be a dominant factor in vegetation growth at an eight-day or seasonal scale in the alpine swamp meadow [109,110]. For example, the observed GPP increased slightly, although the PAR decreased significantly from 2003–2004 (Figures 4d and 5d). Given that the PAR is an important parameter for most GPP models (Table 1), the calculated GPP from the VPM, MVPM, GR, and VI showed significant decreasing tendencies in 2004 relative to 2003 (Figure 7c). Such biases may also occur in the wetlands because their CO_2 flux is mainly controlled by the water depth instead of the PAR at an eight-day or seasonal scale [109].

4.2. Varying Performances of the Eight Satellite-Based GPP Models in the Temperate Steppe

We found large disparities in performance across models in the temperate steppe, agreeing well with previous findings [9,17,18,37,38]. The mean soil water content (0.12 m^3 m^{-3}) was close to the wilting point (0.05–0.07 m^3 m^{-3}) during the growing season, confirming the dominant role of water stress on photosynthesis in the temperate steppe [58,59]. The relatively better performance of the MVPM and VI can be attributed to their better representation of moisture conditions than the other models [9]. The water stress in the MVPM was represented by both VPD and LSWI, reflecting atmospheric water content [9,97,98] and leaf water content [25], respectively. The model performance of the MVPM should therefore be better than that of the LUE models using only LSWI (VPM) or VPD

(MODIS-GPP). For example, the mean value of the water stress scalar in the VPM was 29.4% higher than in the MVPM (0.82 vs. 0.58, respectively), contributing to the overestimation of the modeled GPP by the VPM from 2004 to 2011 (Table 3 and Figure 7a). The water stress in the VI model was represented by the EVI, which was widely documented as the most comprehensive indicator of photosynthetic capacity [39,111]. It thus performed better than the other statistical models using LST (TG), air temperature (AVM), or LSWI (PCM). For instance, the correlation between the observed GPP and the multiplication of environmental factors was also higher in the VI model than in the other four statistical models by 7.8%–22.1% (Figure 8).

Similar to previous studies in grassland and agriculture ecosystems [18,38,88,94], our results indicated that these satellite-based GPP models do not capture all the effects of frequent extreme drought events on vegetation growth in the temperate steppe. The poor model performances in drought years may be due to their failure to address water stress (as discussed above) and the exacerbated effects of severe water stress [62,112]. The interannual variability of grassland carbon flux may be generally caused by both abiotic factors (climate) and biotic factors (ecosystem responses) [113,114]. Severe drought events can amplify ecosystem responses to climate [114]. However, without considering the interrelated physiological and ecological processes, these parametric satellite-based GPP models tend to neglect the effects of ecosystem responses on GPP during drought years [35,36], which can be partially proven by the lower reduction rates of the fPAR (i.e., EVI) and water stress indicators (i.e., LSWI, VPD, and EVI) than the GPP_tower for the two best-performing models (MVPM and VI) during drought years (Figure 4a,b and Figure 5a,b). Worse still, the late response of the vegetation indices to drought-related changes in photosynthesis [100] may lead to an overestimation of the modeled GPP during the periods after the drought events (Figure 5). Consequently, the GPP was clearly overestimated even by these two better models during drought years (Table 3 and Figure 7a). The overestimation would be further exaggerated if the models were calibrated using the normal-year data only, as in previous efforts [8,25,29]. The GPP reduction caused by drought might have been slightly underestimated at the XL site in this study due to ignorance of the possible vegetation recoveries after grazing exclusion [115] (Table 2). It should be noted that although the current water stress indicators, such as EVI, cannot fully capture the GPP responses to drought, they can still be used to monitor the drought effects, especially over large areas where no other information is available [116]. Meanwhile, there is room for future studies to improve the water stress indicators of GPP in the area with extensive data coverage.

4.3. Varying Performances of the Eight Satellite-Based GPP Models in the Alpine Meadow

Performance varied slightly by model in the alpine meadow, which might be related to the accuracy of the input variables or the methods used to address the environmental stresses. For example, the precision of the MODIS-GPP was the lowest in the alpine shrub meadow, primarily due to the uncertainties in the model parameters, such as ε_{max} and fPAR [31,117,118]. The MODIS-GPP algorithm assumed the same ε_{max} for all grassland types, which was 53.7% lower than the ground-based ε_{max} (0.19 vs. 0.41 g C mol^{-1} PPFD, respectively) in the alpine shrub meadow. The mean eight-day MODIS fPAR was 33.2% higher than the fPAR (represented by EVI) used in the other seven models from 2003–2006 (0.43 vs. 0.32, respectively). The performance of the MODIS-GPP algorithm could therefore be greatly improved with site-specific optimized parameters [118]. The GR model exhibited relatively poor performance in the alpine swamp meadow, most likely due to (1) the overweighting of the PAR effects (as discussed in Section 4.1) and (2) the underweighting of environmental stresses on GPP. The environmental stress in the GR model was represented by fPAR (EVI) only, while in all the other models it was represented by both fPAR and LUE scalars. Overall, the intermodel differences of the performances were smaller in the alpine meadow than in the temperate steppe, most likely due to the lower sensitivity of the input variables to the land cover properties in the dense alpine meadow than in the sparse temperate steppe [31,119–121]. For example, the MODIS fPAR tends to overestimate the actual condition [31] of the sparse vegetation due to the background soil conditions.

4.4. Comparisons with Previous Studies on Grassland

The relative model qualities in the alpine meadow, the temperate steppe during non-drought years, and the all-site years from this study were generally consistent with previous studies (Table 5). For example, Li et al. [33] and Niu et al. [122] showed that the AVM performed better than the VPM and PCM in the alpine meadow. Jia et al. [3] and Liu et al. [38] found that the VI and AVM were better than the other models such as the GR, MODIS-GPP, and VPM, in spite of grassland types over northern China. The better performance of the MVPM than the VPM in this study agreed well with our previous study at a global scale [9]. Nevertheless, our findings were different from the previous studies in the temperate steppe during drought years. We showed that the VPM was poorer than the MODIS-GPP and other models (as reflected by AICc), but Liu et al. [123] found the better performance of the VPM than the MODIS-GPP (as reflected by R^2). This may be due to the different indices being used to measure model quality. For example, the VPM was also the best for the temperate steppe in terms of R^2 in this study (Table 3). The better quality of the VPM than the MODIS-GPP was even documented in the global grassland [17]. Studies with more robust statistical measures and more EC observations covering global grasslands are needed to solidify the findings from this study.

Table 5. Comparisons of the findings from this study and previous similar studies on grassland.

Grassland Types	Time Periods	Precipitation Years	Model Performances	Model Performance Indices	Reference
Temperate steppe	2004–2011	Drought	PCM > VI > GR > TG > AVM > MVPM > MODIS-GPP > VPM	R^2, RMSE (%), PBIAS (%), AICc	This study
		Non-drought	MVPM > VI > MODIS-GPP > TG > GR > AVM > PCM > VPM		
		All	VI > MVPM > TG > GR > MODIS-GPP > AVM > PCM > VPM		
Alpine shrub meadow	2003–2006	Non-drought	MVPM > TG > VI > GR > AVM > PCM > VPM > MODIS-GPP		
Alpine swamp meadow	2003–2006	Non-drought	AVM > VPM > TG > MVPM > VI > MODIS-GPP > PCM > GR		
Temperate steppe + alpine meadow	2003–2011	All	MVPM > VI > TG > AVM > GR > MODIS-GPP > PCM > VPM		
Temperate steppe	2006–2007	Drought	VPM > MODIS	R^2, SE	Liu et al. [123]
Alpine meadow	2008–2009	Non-drought	AVM > VPM > TG = VI	R^2	Li et al. [33]
Alpine swamp meadow	2009–2012	Non-drought	AVM > PCM > VPM	R^2	Niu et al. [110]
Temperate steppe + alpine meadow	2003–2005	Non-drought	AVM > TG > VPM > MODIS > GR	R^2, RMSE (%), BIAS	Liu et al. [38]
Temperate steppe + alpine meadow	2003–2013	Non-drought	VI > TG > MODIS > VPM > GR	R^2, ΔAIC	Jia et al. [3]
Global grassland	2000–2007	All	VPM > MODIS	R^2, RMSE	Yuan et al. [17]
Global grassland	2001–2007	All	MVPM > VPM	R^2, RMSE, BIAS	Zhang et al. [9]

ΔAIC: model's AIC minus minimal AIC; SE, standard error.

4.5. Trade-Offs between Model Performance and Applicability at a Regional Scale

The comparisons conducted in this study are based on site-scale observations. However, the model selection at a regional scale needs to consider both the model performance and the availability and accuracy of the input data [27]. More parameters mean more requirements for data input and more in situ data for model calibration, possibly accompanied by worse model performance [27]. Our results showed that the MVPM and VI are the two best-performing models in the northern China grasslands. The MVPM is a typical LUE model. ε_{max} is a key parameter, which is usually represented by a constant for one vegetation type or even an entire eco-region [3,38,86]. Wang et al. [124] suggested that the ε_{max} may vary substantially within a vegetation type due to different species compositions and climate conditions. For example, the ε_{max} at the XL site was 1.9 times that of the NM site, although they are

only 2 km apart (0.57 vs. 0.30 g C mol^{-1} PPFD, respectively). In contrast, the VI model is a typical statistical model that requires in situ data to calibrate the site-specific scalar m (Equation (6)). Due to the limited in situ data, the parameter m was usually indicated by a biome-specific constant [3] or estimated by remote sensing products (e.g., LST_{an}) [28,90], which will lead to poor model performance. For example, we found that the mean R^2 of the VI decreased significantly, by 19.0% (0.79 vs. 0.64), if using the same m (estimated from all the observations) for all four EC sites. Therefore, the choice of the MVPM (LUE model) or VI (statistical model) model depends on the accuracy of ε_{max} and the availability of the EC flux data, respectively.

Further, the varying performance across vegetation subtypes and models confirmed that a single environmental scalar cannot reflect the different responses of vegetation to environmental stresses [3,17,33,34]. This can be further verified by the much-higher explanation ability of multiple variables (76%) than a single factor such as EVI (62%) or LSWI (50%) of the total variance of the observed GPP in the two grassland subtypes (Table 4). Multiple environmental scalars are recommended for future regional applications of satellite-based GPP models, yet caution should be taken regarding the possibility of more uncertainties associated with input environmental variables.

It should be noted that both the optimal models (MVPM and VI) performed relatively poorly in the temperate steppe ($R^2 < 0.68$) and cannot fully account for the effects of extreme drought, which is predicted to occur more frequently in northern China in the future [63,64]. Improving water stress variables to address drought effects, such as incorporating the drought index that can monitor drought in both arid and humid regions [125], constitutes a valid topic worthy of future efforts. Stocker et al. [45] found that model performances can be largely improved by incorporating an estimation of the effects of soil moisture on LUE, particularly during drought years. Other variables and/or the improvements in model structures may also be required due to the complex and nonlinear effects of drought on GPP [9,126].

5. Conclusions

Instead of comparing model performance among different biomes, this study evaluated the performance of eight widely used satellite-based GPP models in vegetation subtypes limited by different environmental factors in a biome. Taking the grasslands in northern China as an example, our results indicated that the performance of the satellite-based GPP models was obviously higher in the temperature-limited alpine meadow than in the water-limited temperate steppe. Additionally, performance varied considerably by model in the temperate steppe due to the different methods being used to address the water stresses. The MVPM and VI in general performed better than the other LUE and statistical models, respectively, owing to their better representation of moisture conditions. The relatively worse model performance in the temperate steppe can be significantly degraded by extreme drought events, regardless of model type. Comparatively, these remote sensing models showed small differences between the alpine shrub meadow and the alpine swamp meadow, except for the relatively worse performances of the MODIS-GPP in the alpine shrub meadow and the GR model in the alpine swamp meadow. Our results highlight the contrasting performances of satellite-based GPP models in grasslands limited by different environmental stresses and in different precipitation years in water-limited areas. Given the varying environmental stresses of different vegetation subtypes [127–129] and the increase in drought events worldwide [63], this study provides important insights for future model improvements and applications. In particular, more effort should be focused on the quantification of the effects of water stress on GPP in water-limited ecosystems and in drought years. Note that the conclusions in this study are based on only four EC flux sites, and further studies incorporating data at more flux sites are needed to see the generality of the findings from this study.

Author Contributions: Conceptualization, L.Z. and D.Z.; methodology, L.Z. and D.Z.; writing—original draft preparation, L.Z.; writing—review and editing, D.Z., J.F., Q.G., S.C., R.W., and Y.L.; supervision, D.Z.

Funding: This research was funded by the National Natural Science Foundation of China (Grant #: 41601196), the National Key R & D Program of China (Grant #: 2017YFA0604804), the Chinese Academy of Sciences

Technology Service Plan (Grant #: KFJ_STS-ZDTP-013-02), the National Natural Science Foundation of China (Grant #: 31870413), and the Qinglan Project of Jiangsu Province of China.

Acknowledgments: We thank the four anonymous reviewers for their valuable comments to improve this manuscript.

Conflicts of Interest: The authors declare no conflict of interest.

Abbreviations

EC	Eddy covariance
PPFD	Photosynthetic photon flux density
NEE	Net ecosystem CO_2 exchange
Re	Ecosystem respiration
GPP	Gross primary productivity
VPM	Vegetation photosynthesis model
MVPM	Modified VPM model
MODIS-GPP	Moderate Resolution Imaging Spectroradiometer GPP algorithm
TG	Temperature and greenness model
GR	Greenness and radiation model
VI	Vegetation index model
AVM	Alpine vegetation model
PCM	Photosynthetic Capacity Model
LUE	Light use efficiency
ε_{max}	Potential LUE without environmental stress
ε_g	Actual LUE
ft	Effects of air temperature on ε_{max}
fw	Effects of water availability on ε_{max}
m	Slope between GPP and environmental scalars
PAR	Photosynthetically active radiation
fPAR	Fraction of PAR absorbed by the vegetation canopy
Ta	Air temperature
VPD	Vapor pressure deficit
EVI	Enhanced vegetation index
LSWI	Land surface water index
LST	Land surface temperature
LST_{an}	Mean annual nighttime LST

References

1. Chapin, F.S., III; Matson, P.A.; Mooney, H.A. *Principles of Terrestrial Ecosystem Ecology*; Springer: New York, NY, USA, 2002; pp. 369–397.
2. Yuan, W.; Liu, S.; Yu, G.; Bonnefond, J.M.; Chen, J.; Davis, K.; Desai, A.R.; Goldstein, A.H.; Gianelle, D.; Rossi, F. Global estimates of evapotranspiration and gross primary production based on modis and global meteorology data. *Remote Sens. Environ.* **2010**, *114*, 1416–1431. [CrossRef]
3. Jia, W.; Liu, M.; Wang, D.; He, H.; Shi, P.; Li, Y.; Wang, Y. Uncertainty in simulating regional gross primary productivity from satellite-based models over northern china grassland. *Ecol. Indic.* **2018**, *88*, 134–143. [CrossRef]
4. Li, Z.; Yu, G.; Xiao, X.; Li, Y.; Zhao, X.; Ren, C.; Zhang, L.; Fu, Y. Modeling gross primary production of alpine ecosystems in the tibetan plateau using modis images and climate data. *Remote Sens. Environ.* **2007**, *107*, 510–519. [CrossRef]
5. Liu, D.; Li, Y.; Wang, T.; Peylin, P.; Macbean, N.; Ciais, P.; Jia, G.; Ma, M.; Ma, Y.; Shen, M. Contrasting responses of grassland water and carbon exchanges to climate change between tibetan plateau and inner Mongolia. *Agric. For. Meteorol.* **2018**, *249*, 163–175. [CrossRef]
6. Baldocchi, D. Measuring fluxes of trace gases and energy between ecosystems and the atmosphere - the state and future of the eddy covariance method. *Glob. Change Biol.* **2014**, *20*, 3600–3609. [CrossRef] [PubMed]
7. Schmid, H.P. Source areas for scalars and scalar fluxes. *Bound.-Lay. Meteorol.* **1994**, *67*, 293–318. [CrossRef]

8. Wu, C.; Niu, Z.; Gao, S. Gross primary production estimation from modis data with vegetation index and photosynthetically active radiation in maize. *J. Geophys. Rese. Atmos.* **2010**, *115*, D12127. [CrossRef]
9. Zhang, L.X.; Zhou, D.C.; Fan, J.W.; Hu, Z.M. Comparison of four light use efficiency models for estimating terrestrial gross primary production. *Ecol. Modell.* **2015**, *300*, 30–39. [CrossRef]
10. Keenan, T.F.; Baker, I.; Barr, A.; Ciais, P.; Davis, K.; Dietze, M.; Dragoni, D.; Gough, C.M.; Grant, R.; Hollinger, D. Terrestrial biosphere model performance for inter-annual variability of land-atmosphere CO_2 exchange. *Glob. Change Biol.* **2012**, *18*, 1971–1987. [CrossRef]
11. Ruimy, A.; Bondeau, L.K. Comparing global models of terrestrial net primary productivity (NPP): Analysis of differences in light absorption and light-use efficiency. *Glob. Change Biol.* **1999**, *5*, 56–64. [CrossRef]
12. Running, S.W.; Coughlan, J.C. A General model of forest ecosystem processes for regional applications i. hydrologic balance, canopy gas exchange and primary production processes. *Ecol. Modell.* **1988**, *42*, 125–154. [CrossRef]
13. Cramer, W.; Kicklighter, D.W.; Bondeau, A.; Iii, B.M.; Churkina, G.; Nemry, B.; Ruimy, A.; Schloss, A.L.; ThE. Participants OF. ThE. Potsdam NpP. Model Intercomparison. Comparing global models of terrestrial net primary productivity (NPP): Overview and key results. *Glob. Change Biol.* **1999**, *5*, 1–15. [CrossRef]
14. Cramer, W.; Bondeau, A.; Woodward, F.I.; Prentice, I.C.; Betts, R.A.; Brovkin, V.; Cox, P.M.; Fisher, V.; Foley, J.A.; Friend, A.D.; et al. Global response of terrestrial ecosystem structure and function to CO_2 and climate change: Results from six dynamic global vegetation models. *Glob. Change Biol.* **2001**, *7*, 357–373. [CrossRef]
15. Knorr, W.; Heimann, M. Uncertainties in global terrestrial biosphere modeling: 1. A comprehensive sensitivity analysis with a new photosynthesis and energy balance scheme. *Global Biogeochem. Cy.* **2001**, *15*, 207–225. [CrossRef]
16. Raupach, M.R.; Rayner, P.J.; Barrett, D.J.; DeFries, R.S.; Heimann, M.; Ojima, D.S.; Quegan, S.; Schmullius, C.C. Model–Data synthesis in terrestrial carbon observation: Methods, data requirements and data uncertainty specifications. *Glob. Change Biol.* **2005**, *11*, 378–397. [CrossRef]
17. Yuan, W.; Cai, W.; Xia, J.; Chen, J.; Liu, S.; Dong, W.; Merbold, L.; Law, B.; Arain, A.; Beringer, J. Global comparison of light use efficiency models for simulating terrestrial vegetation gross primary production based on the LaThuile database. *Agric. For. Meteorol.* **2014**, *192–193*, 108–120. [CrossRef]
18. Dong, J.; Xiao, X.; Wagle, P.; Zhang, G.; Zhou, Y.; Jin, C.; Torn, M.S.; Meyers, T.P.; Suyker, A.E.; Wang, J. Comparison of four evi-based models for estimating gross primary production of maize and soybean croplands and tallgrass prairie under severe drought. *Remote Sens. Environ.* **2015**, *162*, 154–168. [CrossRef]
19. Monteith, J.L. Solar radiation and productivity in tropical ecosystems. *J. Appl. Ecol.* **1972**, *9*, 747–766. [CrossRef]
20. Monteith, J.L. Climate and the efficiency of crop production in britain. *Philos. Trans. Royal Soc. Biol. Sci.* **1977**, *281*, 277–294. [CrossRef]
21. Potter, C.S.; Randerson, J.T.; Field, C.B.; Matson, P.A.; Vitousek, P.M.; Mooney, H.A.; Klooster, S.A. Terrestrial ecosystem production: A process model based on global satellite and surface data. *Global Biogeochem. Cy.* **1993**, *7*, 811–841. [CrossRef]
22. Prince, S.D.; Goward, S.N. Global primary production: A remote sensing approach. *J. Biogeography* **1995**, *22*, 815–835. [CrossRef]
23. Running, S.W.; Nemani, R.; Glassy, J.M.; Thornton, P.E. MODIS daily photosynthesis (PSN) and annual net primary production (NPP) product (MOD17) algorithm theoretical basis document. 2015. Available online: www.ntsg.umt.edu/modis/ATBD/ATBD_MOD17_v21.pdf (accessed on 1 March 2018).
24. Running, S.W.; Thornton, P.E.; Nemani, R.; Glassy, J.M. Global terrestrial gross and net primary productivity from the earth observing system. In *Methods in Ecosystem Science*; Springer: New York, NY, USA, 2000; pp. 44–57.
25. Xiao, X.; Hollinger, D.; Aber, J.; Goltz, M.; Davidson, E.A.; Zhang, Q.; Iii, B.M. Satellite-based modeling of gross primary production in an evergreen needleleaf forest. *Remote Sens. Environ.* **2004**, *89*, 519–534. [CrossRef]
26. Xiao, X.; Zhang, Q.; Braswell, B.; Urbanski, S.; Boles, S.; Wofsy, S.; Iii, B.M.; Ojima, D. Modeling gross primary production of temperate deciduous broadleaf forest using satellite images and climate data. *Remote Sens. Environ.* **2004**, *91*, 256–270. [CrossRef]

27. Yuan, W.; Liu, S.; Zhou, G.; Zhou, G.; Tieszen, L.L.; Baldocchi, D.; Bernhofer, C.; Gholz, H.; Goldstein, A.H.; Goulden, M.L. Deriving a light use efficiency model from eddy covariance flux data for predicting daily gross primary production across biomes. *Agric. For. Meteorol.* **2007**, *143*, 189–207. [CrossRef]
28. Sims, D.A.; Rahman, A.F.; Cordova, V.D.; El-Masri, B.Z.; Baldocchi, D.D.; Bolstad, P.V.; Flanagan, L.B.; Goldstein, A.H.; Hollinger, D.Y.; Misson, L. A new model of gross primary productivity for north american ecosystems based solely on the enhanced vegetation index and land surface temperature from MODIS. *Remote Sens. Environ.* **2008**, *112*, 1633–1646. [CrossRef]
29. Gitelson, A.A.; Viña, A.; Verma, S.B.; Rundquist, D.C.; Arkebauer, T.J.; Keydan, G.; Leavitt, B.; Ciganda, V.; Burba, G.G.; Suyker, A.E. Relationship between gross primary production and chlorophyll content in crops: Implications for the synoptic monitoring of vegetation productivity. *J. Geophys. Res. Atmosp.* **2006**, *111*, D08S11. [CrossRef]
30. Gulbeyaz, O.; Bond-Lamberty, B.; Akyurek, Z.; West, T.O. A New Approach to evaluate the MODIS annual NPP product (MOD17A3) using forest field data from Turkey. *Int. J. Remote Sens.* **2018**, *39*, 2560–2578. [CrossRef]
31. Turner, D.P.; Ritts, W.D.; Cohen, W.B.; Gower, S.T.; Running, S.W.; Zhao, M.; Costa, M.H.; Kirschbaum, A.A.; Ham, J.M.; Saleska, S.R. Evaluation of MODIS NPP and GPP products across multiple biomes. *Remote Sens. Environ.* **2006**, *102*, 282–292. [CrossRef]
32. Sims, D.A.; Rahman, A.F.; Cordova, V.D.; El-Masri, B.Z.; Baldocchi, D.D.; Flanagan, L.B.; Goldstein, A.H.; Hollinger, D.Y.; Misson, L.; Monson, R.K. On the use of MODIS EVI to assess gross primary productivity of north American ecosystems. *J. Geophys. Res. Biogeosci.* **2006**, *111*, 695–702. [CrossRef]
33. Li, F.; Wang, X.; Zhao, J.; Zhang, X.; Zhao, Q. A Method for estimating the gross primary production of alpine meadows using modis and climate data in china. *Inter. J. Remote Sens.* **2013**, *34*, 8280–8300. [CrossRef]
34. Zhang, Y.; Song, C.; Ge, S.; E, B.L.; Asko, N.; Zhang, Q. Understanding moisture stress on light-use efficiency across terrestrial ecosystems based on global flux and remote sensing data. *J. Geophys. Res. Biogeosci.* **2015**, *120*, 2053–2066. [CrossRef]
35. Gunderson, C.A.; O'Hara, K.H.; Campion, C.M.; Walker, A.V.; Edwards, N.T. Thermal plasticity of photosynthesis: The role of acclimation in forest responses to a warming climate. *Glob. Change Biol.* **2010**, *16*, 2272–2286. [CrossRef]
36. Wu, W.X.; Wang, S.Q.; Xiao, X.M.; Yu, G.R.; Fu, Y.L.; Hao, Y.B. Modeling gross primary production of a temperate grassland ecosystem in Inner Mongolia, China, using MODIS imagery and Climate data. *Sci. China* **2008**, *51*, 1501–1512. [CrossRef]
37. Cai, W.; Yuan, W.; Liang, S.; Liu, S.; Dong, W.; Chen, Y.; Liu, D.; Zhang, H. Large differences in terrestrial vegetation production derived from satellite-based Light Use Efficiency models. *Remote Sens.* **2014**, *6*, 8945–8965. [CrossRef]
38. Liu, Z.; Wang, L.; Wang, S. Comparison of different GPP models in China using MODIS image and ChinaFLUX data. *Remote Sens.* **2014**, *6*, 10215–10231. [CrossRef]
39. Gao, Y.; Yu, G.; Yan, H.; Zhu, X.; Li, S.; Wang, Q.; Zhang, J.; Wang, Y.; Li, Y.; Zhao, L. A MODIS-based Photosynthetic Capacity Model to estimate gross primary production in Northern China and the Tibetan Plateau. *Remote Sens. Environ.* **2014**, *148*, 108–118. [CrossRef]
40. Fan, J.; Zhong, H.; Harris, W.; Yu, G.; Wang, S.; Hu, Z.; Yue, Y. Carbon storage in the grasslands of China based on field measurements of above- and below-ground biomass. *Clim. Change* **2008**, *86*, 375–396. [CrossRef]
41. Bao, G.; Bao, Y.; Qin, Z.; Xin, X.; Bao, Y.; Bayarsaikan, S.; Zhou, Y.; Chuntai, B. Modeling net primary productivity of terrestrial ecosystems in the semi-arid climate of the Mongolian Plateau using LSWI-based CASA ecosystem model. *Int. J. Appl. Earth Obs.* **2016**, *46*, 84–93. [CrossRef]
42. Mu, S.; Zhou, S.; Chen, Y.; Li, J.; Ju, W.; Odeh, I.O.A. Assessing the impact of restoration-induced land conversion and management alternatives on net primary productivity in Inner Mongolian grassland, China. *Global Planet. Change* **2013**, *108*, 29–41. [CrossRef]
43. He, H.; Liu, M.; Xiao, X.; Ren, X.; Zhang, L.; Sun, X.; Yang, Y.; Li, Y.; Zhao, L.; Shi, P. Large-scale estimation and uncertainty analysis of gross primary production in Tibetan alpine grasslands. *J. Geophys. Res. Biogeosci.* **2014**, *119*, 466–486. [CrossRef]
44. Wang, X.; Ma, M.; Huang, G.; Veroustraete, F.; Zhang, Z.; Song, Y.; Tan, J. Vegetation primary production estimation for maize and alpine meadow in the Heihe River Basin, China. *Int. J. Appl. Earth Obs.* **2012**, *17*, 94–101. [CrossRef]

45. Stocker, B.D.; Zscheischler, J.; Keenan, T.F.; Prentice, I.C.; Seneviratne, S.I.; Peñuelas, J. Drought impacts on terrestrial primary production underestimated by satellite monitoring. *Nat. Geosci.* **2019**, *12*, 264–270. [CrossRef]
46. Ali, I.; Cawkwell, F.; Dwyer, E.; Barrett, B.; Green, S. Satellite remote sensing of grasslands: From observation to management. *J. Plant Ecol.* **2016**, *9*, 649–671. [CrossRef]
47. Adams, J.M.; Faure, H.; Faure-Denard, L.; McGlade, J.M.; Woodward, F.I. Increases in terrestrial carbon storage from the Last Glacial Maximum to the present. *Nature* **1990**, *348*, 711–714. [CrossRef]
48. Franke, J.; Keuck, V.; Siegert, F. Assessment of grassland use intensity by remote sensing to support conservation schemes. *J. Nat. Conserv.* **2012**, *20*, 125–134. [CrossRef]
49. Melville, B.; Lucieer, A.; Aryal, J. Object-based random forest classification of Landsat ETM+ and WorldView-2 satellite imagery for mapping lowland native grassland communities in Tasmania, Australia. *Int. J. Appl. Earth Obs.* **2018**, *66*, 46–55. [CrossRef]
50. Melville, B.; Lucieer, A.; Aryal, J. Assessing the impact of spectral resolution on classification of lowland native grassland communities based on field spectroscopy in Tasmania, Australia. *Remote Sens.* **2018**, *10*, 308. [CrossRef]
51. Seaquist, J.; Olsson, L.; Ardö, J. A remote sensing-based primary production model for grassland biomes. *Ecol. Modell.* **2003**, *169*, 131–155. [CrossRef]
52. Zhang, L.; Fan, J.; Zhou, D.; Zhang, H. Ecological protection and restoration program reduced grazing pressure in the three-river headwaters region, China. *Rangeland Ecol. Manag.* **2017**, *70*, 540–548. [CrossRef]
53. Li, L.; Fan, W.; Kang, X.; Wang, Y.; Cui, X.; Xu, C.; Griffin, K.L.; Hao, Y. Responses of greenhouse gas fluxes to climate extremes in a semiarid grassland. *Atmos. Environ.* **2016**, *142*, 32–42. [CrossRef]
54. Zhang, L.; Guo, H.; Jia, G.; Wylie, B.; Gilmanov, T.; Howard, D.; Ji, L.; Xiao, J.; Li, J.; Yuan, W. Net ecosystem productivity of temperate grasslands in northern China: An upscaling study. *Agric. For. Meteorol.* **2014**, *184*, 71–81. [CrossRef]
55. Ni, J. Carbon storage in grasslands of China. *J. Arid Environ.* **2002**, *50*, 205–218. [CrossRef]
56. Tang, X.; Zhao, X.; Bai, Y.; Tang, Z.; Wang, W.; Zhao, Y.; Wan, H.; Xie, Z.; Shi, X.; Wu, B. Carbon pools in China's terrestrial ecosystems: New estimates based on an intensive field survey. *Proc. Natl. Acad. Sci. USA* **2018**, *115*, 4021–4026. [CrossRef] [PubMed]
57. NBSC. *China Statistical Yearbook 2008*; Statistics Press: Beijing, China, 2009; pp. 80–87.
58. Fu, Y.; Zheng, Z.; Yu, G.; Hu, Z.; Sun, X.; Shi, P.; Wang, Y.; Zhao, X. Environmental influences on carbon dioxide fluxes over three grassland ecosystems in China. *Biogeosciences* **2009**, *6*, 2879–2893. [CrossRef]
59. Niu, S.; Wu, M.; Han, Y.; Xia, J.; Li, L.; Wan, S. Water-mediated responses of ecosystem carbon fluxes to climatic change in a temperate steppe. *New Phytol.* **2008**, *177*, 209–219. [CrossRef] [PubMed]
60. Guo, Q.; Hu, Z.; Li, S.; Yu, G.; Sun, X.; Zhang, L.; Mu, S.; Zhu, X.; Wang, Y.; Li, Y. Contrasting responses of gross primary productivity to precipitation events in a water-limited and a temperature-limited grassland ecosystem. *Agric. For. Meteorol.* **2015**, *214–215*, 169–177. [CrossRef]
61. Hao, Y.; Kang, X.; Wu, X.; Cui, X.; Liu, W.; Zhang, H.; Li, Y.; Wang, Y.; Xu, Z.; Zhao, H. Is frequency or amount of precipitation more important in controlling CO_2 fluxes in the 30-year-old fenced and the moderately grazed temperate steppe? *Agric., Ecosyst. Environ.* **2013**, *171*, 63–71. [CrossRef]
62. Hao, Y.; Wang, Y.; Mei, X.; Huang, X.; Cui, X.; Zhou, X.; Niu, H. CO_2, H_2O, and energy exchange of an Inner Mongolia steppe ecosystem during a dry and wet year. *Acta Oecol.* **2008**, *33*, 133–143. [CrossRef]
63. Dai, A. Increasing drought under global warming in observations and models. *Nat. Clim. Change* **2013**, *3*, 52–58. [CrossRef]
64. Wang, L.; Chen, W. A CMIP5 multimodel projection of future temperature, precipitation, and climatological drought in China. *Int. J. Climatol.* **2014**, *34*, 2059–2078. [CrossRef]
65. Yu, G.R.; Wen, X.F.; Sun, X.M.; Tanner, B.D.; Lee, X.; Chen, J.Y. Overview of ChinaFLUX and evaluation of its eddy covariance measurement. *Agric. For. Meteorol.* **2006**, *137*, 125–137. [CrossRef]
66. Zhao, M.; Running, S.W.; Nemani, R.R. Sensitivity of Moderate Resolution Imaging Spectroradiometer (MODIS) terrestrial primary production to the accuracy of meteorological reanalyses. *J. Geophys. Res. Biogeosci.* **2006**, *111*, 338–356. [CrossRef]
67. Xiao, X.; Zhang, Q.; Hollinger, D.; Aber, J.; Iii, B.M. Modeling gross primary production of an evergreen needleleaf forest using MODIS and climate data. *Ecol. Appl.* **2005**, *15*, 954–969. [CrossRef]

68. Kalfas, J.L.; Xiao, X.; Vanegas, D.X.; Verma, S.B.; Suyker, A.E. Modeling gross primary production of irrigated and rain-fed maize using MODIS imagery and CO_2 flux tower data. *Agric. For. Meteorol.* **2011**, *151*, 1514–1528. [CrossRef]
69. Xiao, X.; Zhang, Q.; Saleska, S.; Hutyra, L.; Camargo, P.D.; Wofsy, S.; Frolking, S.; Boles, S.; Keller, M.; Iii, B.M. Satellite-based modeling of gross primary production in a seasonally moist tropical evergreen forest. *Remote Sens. Environ.* **2005**, *94*, 105–122. [CrossRef]
70. Running, S.; Mu, Q.; Zhao, M. MOD17A2H MODIS/Terra Gross Primary Productivity 8-Day L4 Global 500m SIN Grid V006. NASA EOSDIS Land Processes DAAC. 2015. [CrossRef]
71. Peng, Y.; Gitelson, A.A. Application of chlorophyll-related vegetation indices for remote estimation of maize productivity. *Agric. For. Meteorol.* **2011**, *151*, 1267–1276. [CrossRef]
72. Peng, Y.; Gitelson, A.A.; Keydan, G.; Rundquist, D.C.; Moses, W. Remote estimation of gross primary production in maize and support for a new paradigm based on total crop chlorophyll content. *Remote Sens. Environ.* **2011**, *115*, 978–989. [CrossRef]
73. Sakamoto, T.; Gitelson, A.A.; Wardlow, B.D.; Verma, S.B.; Suyker, A.E. Estimating daily gross primary production of maize based only on MODIS WDRVI and shortwave radiation data. *Remote Sens. Environ.* **2011**, *115*, 3091–3101. [CrossRef]
74. Wu, C.; Zheng, N.; Quan, T.; Huang, W.; Rivard, B.; Feng, J. Remote estimation of gross primary production in wheat using chlorophyll-related vegetation indices. *Agric. For. Meteorol.* **2009**, *149*, 1015–1021. [CrossRef]
75. Wu, C.; Gonsamo, A.; Gough, C.M.; Chen, J.M.; Xu, S. Modeling growing season phenology in North American forests using seasonal mean vegetation indices from MODIS. *Remote Sens. Environ.* **2014**, *147*, 79–88. [CrossRef]
76. Wang, J.; Cai, Y.C. Studies on genesis, types and characteristics of the soils of the Xilin River Basin. In *Inner Mongolia Grassland Ecosystem Research Station. Research on Grassland Ecosystem*; the Chinese Academy of Sciences, Science Press: Beijing, China, 1988.
77. Song, W.; Wang, H.; Wang, G.; Chen, L.; Jin, Z.; Zhuang, Q.; He, J.S.; Song, W.; Wang, H.; Wang, G. Methane emissions from an alpine wetland on the Tibetan Plateau: Neglected but vital contribution of the nongrowing season. *J. Geophys. Res. Biogeosci.* **2015**, *120*, 1475–1490. [CrossRef]
78. Chen, S.P.; Chen, J.Q.; Lin, G.H.; Zhang, W.L.; Miao, H.X.; Long, W.; Huang, J.H.; Han, X.G.; Sun, G.; Sun, J.X. Energy balance and partition in Inner Mongolia steppe ecosystems with different land use types. *Agric. For. Meteorol.* **2009**, *149*, 1800–1809. [CrossRef]
79. Yu, G.R.; Zhu, X.J.; Fu, Y.L.; He, H.L.; Wang, Q.F.; Wen, X.F.; Li, X.R.; Zhang, L.M.; Zhang, L.; Su, W. Spatial patterns and climate drivers of carbon fluxes in terrestrial ecosystems of China. *Glob. Change Biol.* **2013**, *19*, 798–810. [CrossRef] [PubMed]
80. Zhou, D.; Zhao, S.; Liu, S.; Zhang, L. Spatiotemporal trends of terrestrial vegetation activity along the urban development intensity gradient in China's 32 major cities. *Sci. Total Environ.* **2014**, *488*, 136–145. [CrossRef] [PubMed]
81. Piao, S.; Fang, J.; Zhou, L.; Zhu, B.; Tan, K.; Tao, S. Changes in vegetation net primary productivity from 1982 to 1999 in China. *Global Biogeochem. Cy.* **2005**, *19*, GB2027. [CrossRef]
82. Running, S.; Mu, Q. MOD16A2 MODIS/Terra Net Evapotranspiration 8-Day L4 Global 500m SIN Grid V006. NASA EOSDIS Land Processes DAAC. 2017. [CrossRef]
83. Vermote, E. MOD09A1 MODIS/Terra Surface Reflectance 8-Day L3 Global 500m SIN Grid V006. NASA EOSDIS Land Processes DAAC. 2015. [CrossRef]
84. Wan, Z.; Hook, S.; Hulley, G. MOD11A2 MODIS/Terra Land Surface Temperature/Emissivity 8-Day L3 Global 1km SIN Grid V006. NASA EOSDIS Land Processes DAAC. 2015. [CrossRef]
85. Yuan, W.; Cai, W.; Nguy-Robertson, A.L.; Fang, H.; Suyker, A.E.; Chen, Y.; Dong, W.; Liu, S.; Zhang, H. Uncertainty in simulating gross primary production of cropland ecosystem from satellite-based models. *Agric. For. Meteorol.* **2015**, *207*, 48–57. [CrossRef]
86. Zhao, M.; Heinsch, F.A.; Nemani, R.R.; Running, S.W. Improvements of the MODIS terrestrial gross and net primary production global data set. *Remote Sens. Environ.* **2005**, *95*, 164–176. [CrossRef]
87. Liu, J.F.; Chen, S.P.; Han, X.G. Modeling gross primary production of two steppes in Northern China using MODIS time series and climate data. *Procedia Environ. Sci.* **2012**, *13*, 742–754. [CrossRef]

88. Wagle, P.; Xiao, X.; Torn, M.S.; Cook, D.R.; Matamala, R.; Fischer, M.L.; Jin, C.; Dong, J.; Biradar, C. Sensitivity of vegetation indices and gross primary production of tallgrass prairie to severe drought. *Remote Sens. Environ.* **2014**, *152*, 1–14. [CrossRef]
89. Wang, J.; Xiao, X.; Wagle, P.; Ma, S.; Baldocchi, D.; Carrara, A.; Zhang, Y.; Dong, J.; Qin, Y. Canopy and climate controls of gross primary production of Mediterranean-type deciduous and evergreen oak savannas. *Agric. For. Meteorol.* **2016**, *226–227*, 132–147. [CrossRef]
90. Wu, C.; Gonsamo, A.; Zhang, F.; Chen, J.M. The potential of the greenness and radiation (GR) model to interpret 8-day gross primary production of vegetation. *Isprs J. Photogramm.* **2014**, *88*, 69–79. [CrossRef]
91. Moriasi, D.N.; Arnold, J.G.; Liew, M.W.V.; Bingner, R.L.; Harmel, R.D.; Veith, T.L. Model evaluation guidelines for systematic quantification of accuracy in watershed simulations. *T. Asabe* **2007**, *50*, 885–900. [CrossRef]
92. Symonds, M.R.; Moussalli, A. A brief guide to model selection, multimodel inference and model averaging in behavioural ecology using Akaike's information criterion. *Behav. Ecol. Sociobiol.* **2011**, *65*, 13–21. [CrossRef]
93. Fu, Y.; Yu, G.; Wang, Y.; Li, Z.; Hao, Y. Effect of water stress on ecosystem photosynthesis and respiration of a Leymus chinensis steppe in Inner Mongolia. *Sci. China* **2006**, *49*, 196–206. [CrossRef]
94. Dong, J.; Li, L.; Shi, H.; Chen, X.; Luo, G.; Yu, Q. Robustness and uncertainties of the "Temperature and Greenness" model for estimating terrestrial gross primary production. *Sci. Rep.* **2017**, *7*, 44046. [CrossRef] [PubMed]
95. Hu, Z.; Shi, H.; Cheng, K.; Wang, Y.; Piao, S.; Li, Y.; Zhang, L.; Xia, J.; Zhou, L.; Yuan, W. Joint structural and physiological control on the inter-annual variation in productivity in a temperate grassland: A data-model comparison. *Glob. Change Biol.* **2018**, *24*, 2965–2979. [CrossRef] [PubMed]
96. Schaefer, K.; Schwalm, C.R.; Williams, C.; Arain, M.A.; Barr, A.; Chen, J.M.; Davis, K.J.; Dimitrov, D.; Hilton, T.W.; Hollinger, D.Y. A model-data comparison of gross primary productivity: Results from the North American Carbon Program site synthesis. *J. Geophys. Res.* **2012**, *117*, G03010. [CrossRef]
97. Ding, J.; Yang, T.; Zhao, Y.; Liu, D.; Wang, X.; Yao, Y.; Peng, S.; Wang, T.; Piao, S. Increasingly important role of atmospheric aridity on Tibetan alpine grasslands. *Geophys. Res. Lett.* **2018**, *45*, 2852–2859. [CrossRef]
98. Zhao, M.; Running, S.W. Drought-induced reduction in global terrestrial net primary production from 2000 through 2009. *Science* **2010**, *329*, 940–943. [CrossRef] [PubMed]
99. Chandrasekar, K.; Sesha Sai, M.; Roy, P.; Dwevedi, R. Land Surface Water Index (LSWI) response to rainfall and NDVI using the MODIS Vegetation Index product. *Int. J. Remote Sens.* **2010**, *31*, 3987–4005. [CrossRef]
100. Liu, L.; Yang, X.; Zhou, H.; Liu, S.; Zhou, L.; Li, X.; Yang, J.; Han, X.; Wu, J. Evaluating the utility of solar-induced chlorophyll fluorescence for drought monitoring by comparison with NDVI derived from wheat canopy. *Sci. Total Environ.* **2018**, *625*, 1208–1217. [CrossRef] [PubMed]
101. Lee, J.E.; Frankenberg, C.; Tol, C.V.D.; Berry, J.A.; Guanter, L.; Boyce, C.K.; Fisher, J.B.; Morrow, E.; Worden, J.R.; Asefi, S. Forest productivity and water stress in Amazonia: Observations from GOSAT chlorophyll fluorescence. *Proc. R. Soc. B* **2013**, *280*, 176–188. [CrossRef] [PubMed]
102. Gu, Y.; Brown, J.F.; Verdin, J.P.; Wardlow, B. A five-year analysis of MODIS NDVI and NDWI for grassland drought assessment over the central Great Plains of the United States. *Geophys. Res. Lett.* **2007**, *34*, L06407. [CrossRef]
103. Wang, L.; Qu, J.J. NMDI: A normalized multi-band drought index for monitoring soil and vegetation moisture with satellite remote sensing. *Geophys. Res. Lett.* **2007**, *34*, L20405. [CrossRef]
104. Chaves, M.M.; Pereira, J.S.; Maroco, J.; Rodrigues, M.L.; Ricardo, C.P.P.; Osório, M.L.; Carvalho, I.; Faria, T.; Pinheiro, C. How plants cope with water stress in the field? Photosynthesis and growth. *Ann. Bot.* **2002**, *89*, 907–916. [CrossRef]
105. Bréda, N.; Huc, R.; Granier, A.; Dreyer, E. Temperate forest trees and stands under severe drought: A review of ecophysiological responses, adaptation processes and long-term consequences. *Ann. For. Sci.* **2006**, *63*, 625–644. [CrossRef]
106. Li, N.; Wang, G.; Yang, Y.; Gao, Y.; Liu, G. Plant production, and carbon and nitrogen source pools, are strongly intensified by experimental warming in alpine ecosystems in the Qinghai-Tibet Plateau. *Soil Biol. Biochem.* **2011**, *43*, 942–953.
107. Wang, Z.Y.; Sun, G.; Wang, J. A study of soil-dynamics based on a simulated drought in an alpine meadow on the Tibetan Plateau. *J. Mt. Sci.* **2013**, *10*, 833–844. [CrossRef]

108. Xu, M.; Peng, F.; You, Q.; Guo, J.; Tian, X.; Xue, X.; Liu, M. Year-round warming and autumnal clipping lead to downward transport of root biomass, carbon and total nitrogen in soil of an alpine meadow. *Environ. Exp. Bot.* **2015**, *109*, 54–62. [CrossRef]
109. Hirota, M.; Tang, Y.; Hu, Q.; Hirata, S.; Kato, T.; Mo, W.; Cao, G.; Mariko, S. Carbon dioxide dynamics and controls in a deep-water wetland on the qinghai-tibetan plateau. *Ecosystems* **2006**, *9*, 673–688. [CrossRef]
110. Niu, B.; He, Y.; Zhang, X.; Du, M.; Shi, P.; Sun, W.; Zhang, L. CO_2 exchange in an alpine swamp meadow on the central Tibetan Plateau. *Wetlands* **2017**, *37*, 525–543. [CrossRef]
111. Huete, A.; Didan, K.; Miura, T.; Rodriguez, E.P.; Gao, X.; Ferreira, L.G. Overview of the radiometric and biophysical performance of the MODIS vegetation indices. *Remote Sens. Environ.* **2002**, *83*, 195–213. [CrossRef]
112. Granier, A.; Reichstein, M.; Bréda, N.; Janssens, I.A.; Falge, E.; Ciais, P.; Grünwald, T.; Aubinet, M.; Berbigier, P.; Bernhofer, C. Evidence for soil water control on carbon and water dynamics in European forests during the extremely dry year: 2003. *Agric. For. Meteorol.* **2007**, *143*, 123–145. [CrossRef]
113. Marcolla, B.; Cescatti, A.; Manca, G.; Zorer, R.; Cavagna, M.; Fiora, A.; Gianelle, D.; Rodeghiero, M.; Sottocornola, M.; Zampedri, R. Climatic controls and ecosystem responses drive the inter-annual variability of the net ecosystem exchange of an alpine meadow. *Agric. For. Meteorol.* **2011**, *151*, 1233–1243. [CrossRef]
114. Zhang, T.; Zhang, Y.; Xu, M.; Xi, Y.; Zhu, J.; Zhang, X.; Wang, Y.; Li, Y.; Shi, P.; Yu, G. Ecosystem response more than climate variability drives the inter-annual variability of carbon fluxes in three Chinese grasslands. *Agric. For. Meteorol.* **2016**, *225*, 48–56. [CrossRef]
115. Li, Y.; Fan, J.; Yu, H. Grazing Exclusion, a Choice between Biomass Growth and Species Diversity Maintenance in Beijing—Tianjin Sand Source Control Project. *Sustainability* **2019**, *11*, 1941. [CrossRef]
116. Kath, J.; Le Brocque, A.F.; Reardon-Smith, K.; Apan, A. Remotely sensed agricultural grassland productivity responses to land use and hydro-climatic drivers under extreme drought and rainfall. *Agric. For. Meteorol.* **2019**, *268*, 11–22. [CrossRef]
117. Fu, G.; Zhang, J.; Shen, Z.-X.; Shi, P.-L.; He, Y.-T.; Zhang, X.-Z. Validation of collection of 6 MODIS/Terra and MODIS/Aqua gross primary production in an alpine meadow of the Northern Tibetan Plateau. *Int. J. Remote Sens.* **2017**, *38*, 4517–4534. [CrossRef]
118. Niu, B.; He, Y.; Zhang, X.; Fu, G.; Shi, P.; Du, M.; Zhang, Y.; Zong, N. Tower-based validation and improvement of MODIS gross primary production in an alpine swamp meadow on the Tibetan Plateau. *Remote Sens.* **2016**, *8*, 592. [CrossRef]
119. Turner, D.P.; Ollinger, S.; Smith, M.-L.; Krankina, O.; Gregory, M. Scaling net primary production to a MODIS footprint in support of Earth observing system product validation. *Int. J. Remote Sens.* **2004**, *25*, 1961–1979. [CrossRef]
120. Sims, D.A.; Luo, H.; Hastings, S.; Oechel, W.C.; Rahman, A.F.; Gamon, J.A. Parallel adjustments in vegetation greenness and ecosystem CO_2 exchange in response to drought in a Southern California chaparral ecosystem. *Remote Sens. Environ.* **2006**, *103*, 289–303. [CrossRef]
121. Liu, Z.; Shao, Q.; Liu, J. The Performances of MODIS-GPP and -ET Products in China and Their Sensitivity to Input Data (FPAR/LAI). *Remote Sens.* **2015**, *7*, 135–152. [CrossRef]
122. Niu, B.; Zhang, X.; He, Y.; Shi, P.; Fu, G.; Du, M.; Zhang, Y.; Zong, N.; Zhang, J.; Wu, J. Satellite-based estimation of gross primary production in an alpine swamp meadow on the tibetan plateau: A multi-model comparison. *J. Resour. Ecol.* **2017**, *8*, 57–67.
123. Liu, J.; Sun, O.J.; Jin, H.; Zhou, Z.; Han, X. Application of two remote sensing GPP algorithms at a semiarid grassland site of North China. *J. Plant Ecol.* **2011**, *4*, 302–312. [CrossRef]
124. Wang, H.; Jia, G.; Fu, C.; Feng, J.; Zhao, T.; Ma, Z. Deriving maximal light use efficiency from coordinated flux measurements and satellite data for regional gross primary production modeling. *Remote Sens. Environ.* **2010**, *114*, 2248–2258. [CrossRef]
125. Rhee, J.; Im, J.; Carbone, G.J. Monitoring agricultural drought for arid and humid regions using multi-sensor remote sensing data. *Remote Sens. Environ.* **2010**, *114*, 2875–2887. [CrossRef]
126. Zheng, Y.; Zhang, L.; Xiao, J.; Yuan, W.; Yan, M.; Li, T.; Zhang, Z. Sources of uncertainty in gross primary productivity simulated by light use efficiency models: Model structure, parameters, input data, and spatial resolution. *Agric. For. Meteorol.* **2018**, *263*, 242–257. [CrossRef]

127. Fu, Y.-L.; Yu, G.-R.; Sun, X.-M.; Li, Y.-N.; Wen, X.-F.; Zhang, L.-M.; Li, Z.-Q.; Zhao, L.; Hao, Y.-B. Depression of net ecosystem CO_2 exchange in semi-arid Leymus chinensis steppe and alpine shrub. *Agric. For. Meteorol.* **2006**, *137*, 234–244. [CrossRef]
128. Lindroth, A.; Grelle, A.; Morén, A.S. Long-term measurements of boreal forest carbon balance reveal large temperature sensitivity. *Glob. Change Biol.* **1998**, *4*, 443–450. [CrossRef]
129. Maselli, F.; Papale, D.; Puletti, N.; Chirici, G.; Corona, P. Combining remote sensing and ancillary data to monitor the gross productivity of water-limited forest ecosystems. *Remote Sens. Environ.* **2009**, *113*, 657–667. [CrossRef]